

SYNTHETIC APERTURE RADAR INTERFEROMETRY TO MEASURE EARTH'S SURFACE TOPOGRAPHY AND ITS DEFORMATION

Roland Bürgmann¹, Paul A. Rosen², and Eric J. Fielding³

¹*University of California, Berkeley, Department of Geology and Geophysics, 301
McCone Hall, Berkeley, California 94720; e-mail: burgmann@seismo.berkeley.edu;*

²*Mail Stop 300–235, Jet Propulsion Laboratory, California Institute of Technology, 4800
Oak Grove Drive, Pasadena, California 91109;* ³*Mail Stop 300–233, Jet Propulsion
Laboratory, California Institute of Technology, 4800 Oak Grove Drive, Pasadena,
California 91109; also at: Department of Earth Sciences, University of Oxford, Parks
Road, Oxford OX1 3PR, United Kingdom*

Key Words remote sensing, crustal deformation, earthquakes, volcanoes, land
subsidence, topography

■ **Abstract** Synthetic aperture radar interferometry (InSAR) from Earth-orbiting spacecraft provides a new tool to map global topography and deformation of the Earth's surface. Radar images taken from slightly different viewing directions allow the construction of digital elevation models of meter-scale accuracy. These data sets aid in the analysis and interpretation of tectonic and volcanic landscapes. If the Earth's surface deformed between two radar image acquisitions, a map of the surface displacement with tens-of-meters resolution and subcentimeter accuracy can be constructed. This review gives a basic overview of InSAR for Earth scientists and presents a selection of geologic applications that demonstrate the unique capabilities of InSAR for mapping the topography and deformation of the Earth.

INTRODUCTION

In the course of a little more than two decades, InSAR (interferometric synthetic aperture radar) has developed from theoretical concept to a technique that is revolutionizing a wide range of Earth science fields. Considering that none of the currently deployed imaging radar satellite platforms was designed with interferometric applications in mind, the high quality and vast quantity of exciting results from this technique are astounding. A number of reviews on theory and applications of InSAR have been written (Griffiths 1995, Gens & Vangenderen 1996, Bamler & Hartl 1998, Massonnet & Feigl 1998, Madsen & Zebker 1999, Rosen

et al 2000). Here, we focus on providing a basic overview of InSAR for Earth scientists and present a selection of geologic applications that demonstrate the unique capabilities of InSAR for mapping the topography and deformation of the Earth. We do not attempt to give a comprehensive review of the technical and mathematical details that are essential to producing SAR images and InSAR measurements.

Numerous studies that have been published in recent years illustrate the unique contributions InSAR can make to the Earth sciences. Our review of its applications highlights a few studies of topography and surface deformation, with an emphasis on results that would have been difficult to accomplish without the unique capabilities of InSAR. We discuss applications of InSAR in the fields of crustal deformation research, including surface displacements from tectonic deformation, volcanism, and subsurface fluid flow. However, InSAR is also used in many other fields. For brief introductions to studies of ocean currents, vegetation parameters, terrain classifications, glacial processes, and landslides we refer the reader to Rosen et al (2000) and Massonnet & Feigl (1998). We hope this presentation will stimulate those in the Earth science community who have not yet experienced the excitement of “fringes” appearing before them on their computer screen, revealing a new detailed picture of a distant event. As the community embraces this technology, new applications and ideas that have not yet been considered will arise. New SAR satellite systems currently in production or on the drawing boards promise a rich source of high-quality interferometric data.

SAR—HOW IT WORKS

Conventional radar (radio detection and ranging) imaging is a technique in which a target is illuminated with electromagnetic waves of microwave frequency and the reflected signal is used to deduce information about the target. The all-weather, transmit-and-receive, radar imaging remote sensing technique uses the round-trip travel times and amplitude of the signal reflected from multiple targets on the ground to determine the distances to the targets, and to generate a rough two-dimensional image of the target area as the radar sweeps the area of interest. Bright regions in a radar image represent high amplitude of the returned wave energy, which depends on the surface slope and roughness and the dielectric characteristics of the surface material. Such a real-aperture radar in space would have a resolution of about 5–10 km, limited by the power and size of the footprint of the radar beam, and thus would be of little use for solid-earth remote sensing applications. SAR (synthetic aperture radar) combines signal processing techniques with satellite orbit information to produce a much-higher-resolution (tens of meters) radar image.

SAR processing significantly improves the resolution of point targets in both the cross-track (range) and along-track (azimuth) direction by focusing the raw radar echoes (Elachi 1988, Curlander & McDonough 1991). Fine resolution in

the cross-track direction is achieved by using a radar signal of high bandwidth, which improves the differentiation of radar echoes from closely spaced targets in the range direction. Focusing in the along-track direction relies on the synthetic aperture provided by a moving antenna. The radar return from a particular point target on the ground is present in successively recorded radar echoes (note that the radar footprints of successive pulses overlap). As the moving antenna passes by the image point, the Doppler frequency shift of the return signal from the point and the round trip time of the signal can be used together to differentiate image points in the azimuth direction. Because the Doppler frequency shift depends on the location of the target fore or aft of the radar beam's center, the frequency of the return from the target sweeps out a band as the target passes through the radar's footprint. With this information, a signal of high bandwidth is constructed in the azimuth direction using successive pulses of the radar. The echoes are combined to synthesize a larger antenna aperture or size and thus achieve much improved resolution. A typical image point (pixel) spacing in space-based SAR images is 20–100 m within a 100-km-wide swath.

INSAR—HOW IT WORKS

Two SAR images can be combined to produce a radar interferogram, which can reveal information about the third dimension (elevation) of the target area or measure minute changes in the range distance between two image acquisitions. After SAR focusing, the radar image is a two-dimensional record of both the amplitudes and the phases of the returns from targets within the imaging area. The amplitude is a measure of target reflectivity, whereas the phase encodes changes at the surface as well as a term proportional to the range to the target. InSAR uses the phase information in two SAR images to determine the phase difference between each pair of corresponding image points, thus producing an interferogram. Thus, if two SAR images of a target area are available and can be precisely aligned to a fraction of a pixel width, the relative phase of each image point can be determined. Relative phase data from two images taken from slightly different viewing angles provide information about changes in range to targets on the ground, and thus the surface topography at the resolution of the SAR image can be recovered with knowledge of the imaging geometry. Interestingly, the first applications of InSAR were in Earth-based studies of topography of the Moon and Venus (Zisk 1972, Rumsey et al 1974).

The phase difference of two images taken from the same viewpoint, but at different times, can precisely measure any shifts of the returned phase. Thus, if the Earth's surface moved toward or away from the radar between the two imaging passes, phase changes would result that can be measured with a precision corresponding to millimeter-level displacements. The first demonstration of this technique used Seasat satellite data to detect vertical motions caused by soil swelling

of irrigated fields in the Imperial Valley, California (Gabriel et al 1989). In the following section we give a more detailed explanation of how InSAR can be used to measure Earth's topography and its deformation through time.

Measuring Topography

Digital elevation models (DEMs) are regularly gridded representations of a region's topography. InSAR methods for determination of topographic DEMs vary slightly depending on the geometry of the transmitting and receiving antennas. Systems designed for topographic applications commonly use a configuration of two antennas on the same platform (Graham 1974, Zebker & Goldstein 1986). One antenna emits a microwave signal whose backscattered energy is received by it and an additional antenna located at a fixed distance. Dual antennas are commonly used on aircraft mounted systems, such as NASA's TOPSAR (Topographic SAR) (Evans et al 1993). The Shuttle Radar Topography Mission (SRTM), to be launched in January of 2000, is dedicated to the production of a precise global DEM and will use a receiving antenna located on a boom extended 60 m from the primary antenna on the shuttle. Most spaceborne systems rely on single-antenna satellites, such that the spacecraft must closely repeat the initial orbit to produce a second SAR image for interferometry. The tandem mission of the European Space Agency (ESA) ERS-1 and ERS-2 spacecraft had the two satellites follow each other along the same orbit, so that a common area was imaged at 1-day time separation to allow for the generation of topographic maps. For consistency with the treatment of surface deformation measurements, we only describe the latter configuration, called repeat-track or dual-pass interferometry.

Figure 1 shows the geometry for repeat-track interferometry. Our goal is to determine the elevation h of each image point from the two SAR images. The radar carrier wavelength λ is known from the radar system design. The satellite flight height H and orbit separation vector \vec{B} can be estimated from precise satellite orbits. The initial satellite-to-image point range distance ρ_1 along the look vector \vec{l}_1 is determined from the radar signal delay, and the relative difference between the two phase measurements ϕ is our interferogram.

We assume that no changes in surface properties, surface elevation, or atmospheric path delay occurred during the short time interval between the two satellite passes. The phase of each point in one radar image is the sum of the propagation phase, proportional to ρ , and the phase of the area-integrated phase return from the respective pixel area, which varies randomly between pixels. If the backscatter phase does not change, the measured phase difference between the two images ϕ is due only to differences in the propagation phase, which is proportional to the difference in path delay given by $\phi = 4\pi/\lambda(\rho_2 - \rho_1)$, where $\rho_{1,2}$ is the range from antenna $A_{1,2}$ to the image point on the Earth's surface. The propagation phase difference depends on the geometry of the two antenna tracks and the image point (Figure 1). Thus, if the antenna configuration (baseline separation vector

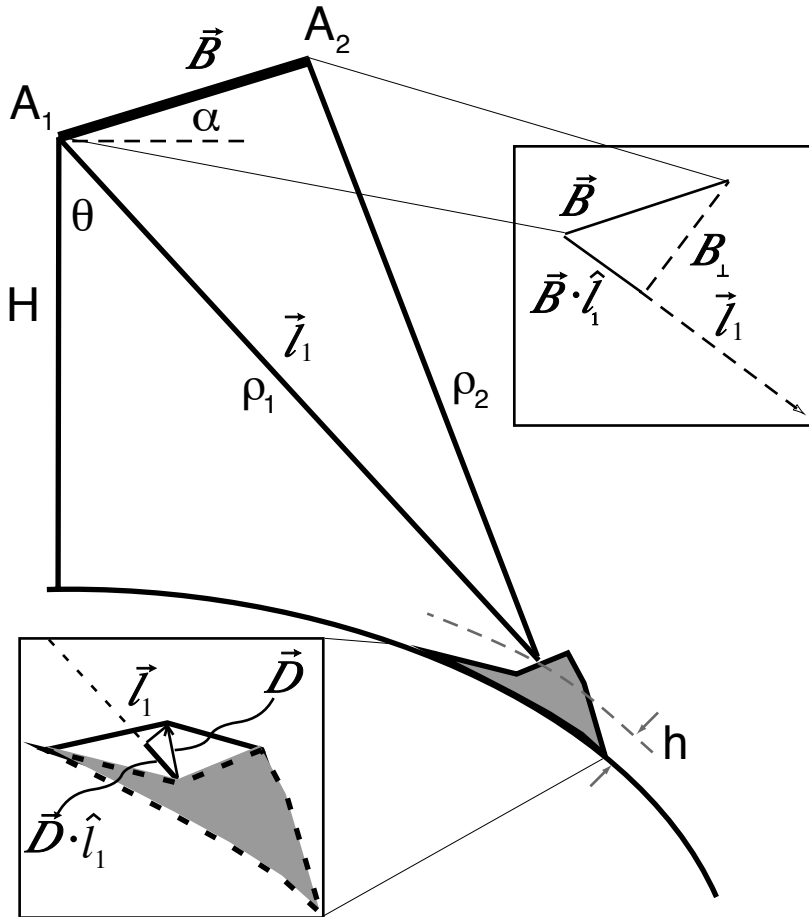


Figure 1 Imaging geometry of side-looking radar for InSAR applications. The *box* in the *top right* illustrates the contribution of the orbit separation baseline to measured range differences. The *box* in the *bottom left* illustrates the range change caused by the surface displacement component in the range direction. See text for discussion and explanation.

\vec{B} and range distance ρ_1) is well known, the phase difference allows for the determination of the target region's topography. This approach is similar to the determination of topography using stereoscopic analysis of standard photographic images.

The point-wise product of one image with the complex conjugate of the other is called an interferogram, the phase of which is a fringe pattern that represents the difference in propagation phase of the two SAR images described previously. This phase difference can only be determined modulo 2π . The interferogram

amplitude (brightness) is the product of the image backscatter amplitudes. Interferograms are often displayed overlaying the brightness rendered in grayscale, and phase as color, where each cycle of color, or fringe, represents a phase change of 2π radians.

Differences in range distance can be determined by multiplying the relative phase differences in units of cycles by the wavelength of the radar signal. To determine the image point's position we require the orbit information, information about the baseline vector separating the two imaging antenna positions, and the interferometric range.

The interferometric phase is (Rosen et al 2000)

$$\phi = 4\pi\rho_1/\lambda[1 - 2(\vec{B} \cdot \hat{l}_1)/\rho_1 + (B/\rho_1)^2 - 1], \quad (1)$$

where \hat{l}_1 is the unit vector in the range direction and \vec{B} is the baseline separation vector of length B . If the baseline length is $B \ll \rho_{1,2}$ we can apply a parallel ray approximation (Zebker & Goldstein 1986) and simplify Equation 1 to $\phi \approx -4\pi/\lambda \cdot (\vec{B} \cdot \hat{l}_1) = -4\pi/\lambda \cdot B \cdot \sin(\theta - \alpha)$ (Figure 1). That is, the interferometric phase is approximately proportional to the projection of the antenna baseline vector on the look direction (Zebker & Goldstein 1986). With our phase measurement, the known radar wavelength, and the geometry shown in Figure 1, we can determine $\theta = \sin^{-1}(-\lambda\phi/4\pi B) + \alpha$, and the surface elevation is then $h = H - \rho_1 \cos\theta$.

The natural variation of the line-of-sight vector across a scene leads to a large gradient of phase across an image. This phase gradient across an interferogram is removed by “flattening” the interferogram. In this process we remove the expected phase produced by a surface of constant elevation on a spherical Earth.

The total phase difference between two image points in an interferogram, which may measure many multiples of 2π , needs to be determined by counting the number of phase cycles, or fringes, between the points. This crucial step in the interferogram determination is called phase unwrapping, which has been the focus of a variety of approaches and algorithm development (e.g. Zebker & Lu 1998). Height information as determined from the interferometric phase, together with the two-dimensional positions on the Earth's surface determined using SAR analysis techniques, allows for the construction of a DEM of the scenes' topography.

To describe the effect of the satellite orbital separation on the interferometric phase, it is convenient to define the ambiguity height h_a , the elevation difference that leads to a full 2π change in phase

$$h_a = 2\pi \cdot \partial h / \partial \phi = (\lambda\rho_1 \sin \theta) / 2B \cdot \cos(\theta - \alpha), \quad (2)$$

where $B \cdot \cos(\theta - \alpha)$ is the component of the antenna baseline perpendicular to the range direction, or B_{\perp} (Figure 1).

Measuring Surface Displacements

Using the same repeat-track imaging geometry described in the previous section, it is apparent that if images are taken at different times, and an image point displaces in the direction of the range vector, an additional phase difference results (Goldstein & Zebker 1987, Gabriel et al 1989, Goldstein et al 1993, Massonnet et al 1993). If the second image is taken from the identical antenna position as the first, the observed phase difference should result solely from the motion of the image point toward or away from the antenna (neglecting differences in signal delay through the atmosphere, discussed below).

In most deformation interferograms, however, we are faced with both topographic and deformation effects. We can express the contribution of a surface displacement vector \vec{B} of the image point to the interferometric phase

$$\phi \approx 4\pi/\lambda(-\vec{B} \cdot \hat{l}_1) + (\vec{D} \cdot \hat{l}_1), \quad (3)$$

assuming that the baseline and displacement vectors are significantly less than the range distance. Surface displacement and resulting range change $\delta\rho$ are related as $\delta\rho = \vec{D} \cdot \hat{l}_1$ (Figure 1). A displacement in the range direction $\delta\rho$ of $\lambda/2$ gives one cycle of phase difference or one fringe. For the ERS microwave C-band (5.2 GHz) radar, this corresponds to a motion of 28 mm. For comparison, we recall that to produce a topographic fringe the elevation must change by the ambiguity height h_a for one cycle of phase. For an ERS perpendicular radar baseline of 100 m, this corresponds to an elevation difference of roughly 100 m.

InSAR measures a change in range along the look direction but is not capable of determining the full three-dimensional displacement vector. To measure an additional component of the displacement vector, we can combine information from interferograms from both ascending (moving north) and descending (moving south) satellite orbit tracks, or integrate data from multiple spacecrafts.

Because current satellites repeat their orbits only within several hundred meters, radar interferograms commonly contain both topographic information as well as surface motions. To separate out the contribution of topography, we need to remove topographic fringes, either through an independently determined DEM (e.g. Massonnet et al 1993) or using InSAR to correct for the topography, as described above (e.g. Zebker et al 1994). In the latter case, at least three images are required (three-pass method). One pair that does not include deformation is used to remove the topographic phase differences from the pair that also includes surface deformation (Gabriel et al 1989).

Producing Interferograms and Derived Geophysical Measurements

The interferogram, which is the basic interferometric measurement, is formed from two full-resolution SAR images. The SAR images are naturally complex quantities; the amplitude of each pixel of a SAR image represents the backscatter

amplitude, and the phase of each pixel is the sum of the two-way propagation phase delay and the contribution from scatterers within the pixel. The scatterer phase is generally random from pixel to pixel because the spatial distribution of scatterers on the ground is random.

The production of an interferogram is in principle a straightforward procedure (Figure 2). The first step is to obtain two SAR images at full resolution in complex form. Ancillary information specifying time reference and intervals of each image and image processing parameters such as the assumed pointing of the radar antenna (this can be arbitrarily chosen in the processing within the angular extent of the antenna beam) and chosen resolutions are also needed. Space agencies that acquire satellite SAR data traditionally have provided the service of generating complex imagery for the user community, often with processing parameters specified by the user. A recent trend in processing for interferometry has been for users to order unprocessed data from the space agency archives and process it themselves; this allows for greater control of the phase to ensure geometric interpretability of the interferogram, and for greater flexibility to reprocess data.

The second step in interferogram formation determines the mapping of pixel locations of common features from one image to the other, accounting for shifts and distortions of the source images arising from the geometry and inherent system limitations. The relative range to a feature in two images depends on the baseline and the topography. This can be seen from Equation 1, where the range difference encoded in the interferogram phase is precisely the range distortion of one image with respect to the other. For small baselines, the topographic variations introduce only a small modulation of this range difference and can be ignored. Even so, there remains a systematic relative range distortion across the image that must be taken into account. Because of subtle differences in spacecraft velocity from one orbit to another, there often remains a systematic along-track distortion as well. The features must be aligned to a small fraction of a pixel, typically better than $100 \mu\text{s}$ ($<1 \text{ m}$) along-track and 5 ns ($<1 \text{ m}$) in range for a $5 \text{ m} \times 8 \text{ m}$ ERS pixel. Without this alignment, the random backscatter phase contribution from each collection of scatterers does not destructively cancel in forming the interferogram.

To process data automatically using only a priori information, the absolute timing both along-track and in range in an absolute sense, as well as some knowledge of the height of the surface, must be known more accurately than what is currently provided by spaceborne sensors. As a result, accurate estimates of image alignment must use cross-correlations of the common features themselves. This is usually done on a regular grid across the image. In each grid intersection, a local value of the co-registration offset can be estimated by amplitude cross-correlation of the two complex images.

Once the co-registration distortion is determined, the third step is to form the interferogram. This is usually done by resampling one of the complex images to match the other, according to the co-registration prescription. Since the distortion

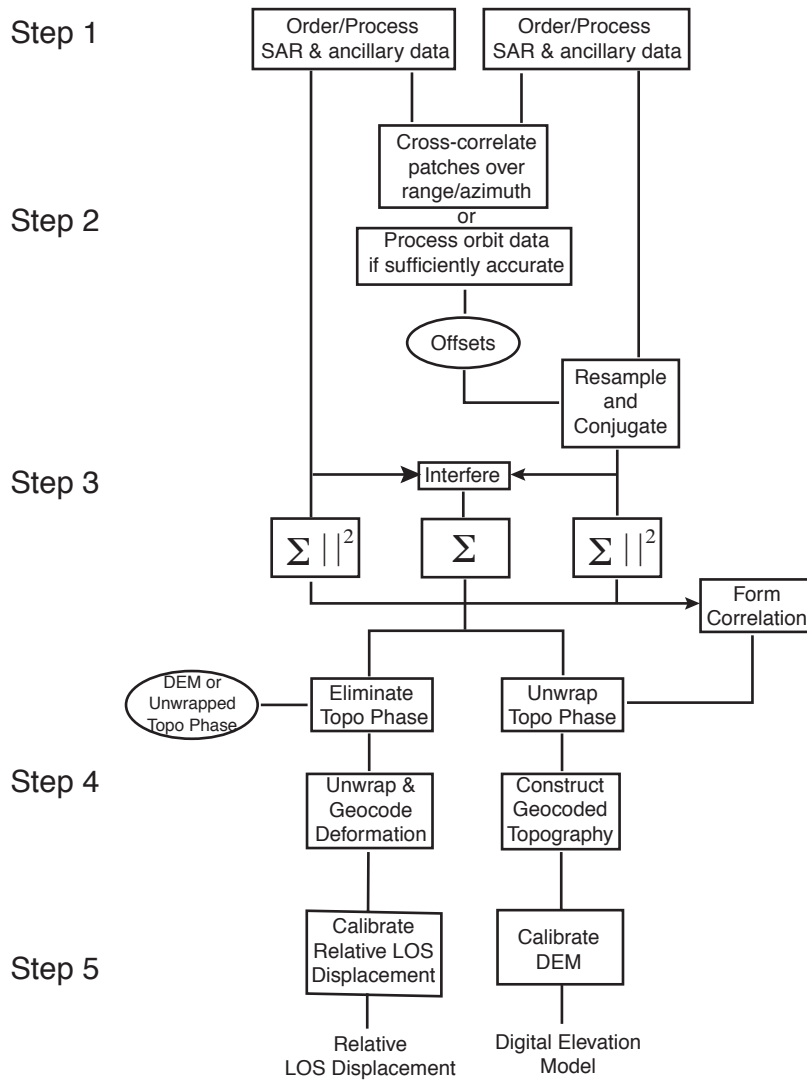


Figure 2 Schematic of steps in processing SAR data for interferometric applications. Step 1 entails ordering, cleaning, and processing SAR data and ancillary data. Step 2 determines the coregistration offsets between the images. If orbits are accurate to 1/20 pixel, this can be done without using the SAR data. If not, the SAR data are cross-correlated to determine the offsets. Step 3 resamples and forms the interferogram and correlation. The *outer boxes* with the summation symbols in this step represent averaging the power of nearby pixels. The *center summation box* represents averaging the interferogram. These averages are required to estimate the correlation (see text). Step 4 unwraps the phase and produces the geophysical measurement. Step 5 is calibration of the measurement.

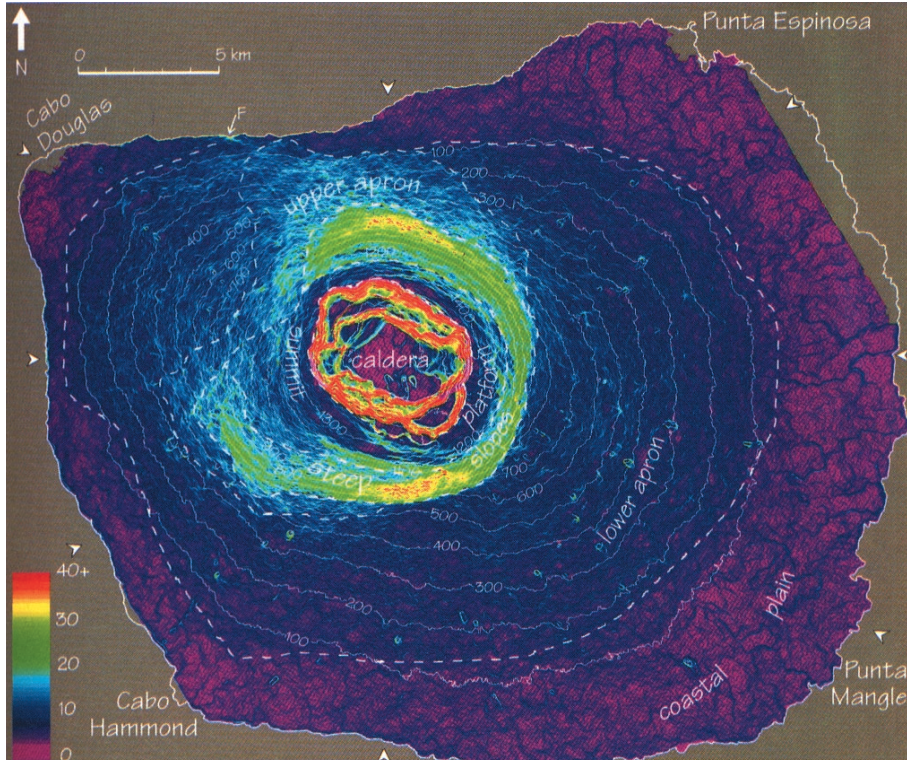


Figure 4 Slope map derived from TOPSAR DEM mosaic for Isla Fernandina, Galapagos. Contour interval is 100 m, and the coastline is marked with a *solid white line*. *Dashed lines* separate slope regions on the Fernandina volcano. The region of steep slopes is unusual for basaltic shield volcanoes outside of the Galapagos (after Rowland 1996).

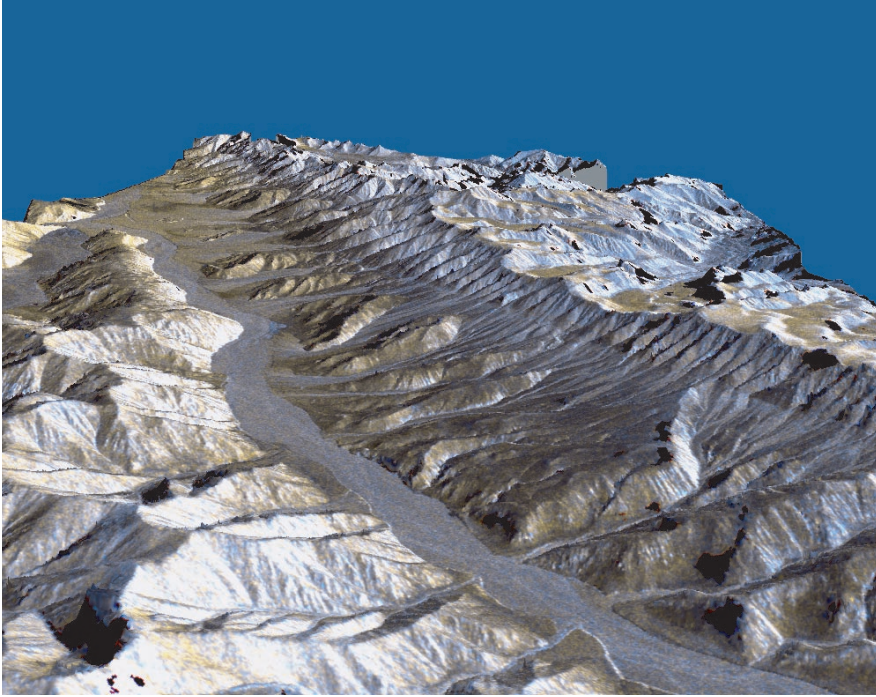


Figure 5 Three-dimensional perspective view of Karakax valley DEM. Elevation is shown without vertical exaggeration with the SIR-C radar images overlain. The L-band amplitude is assigned to red, L- and C-band (24 and 6 cm wavelengths) average to green, and C-band to blue. The active strand of the Altyn Tagh fault is visible as a sharp break in slope running diagonally up the valley side (after Fielding 1999).

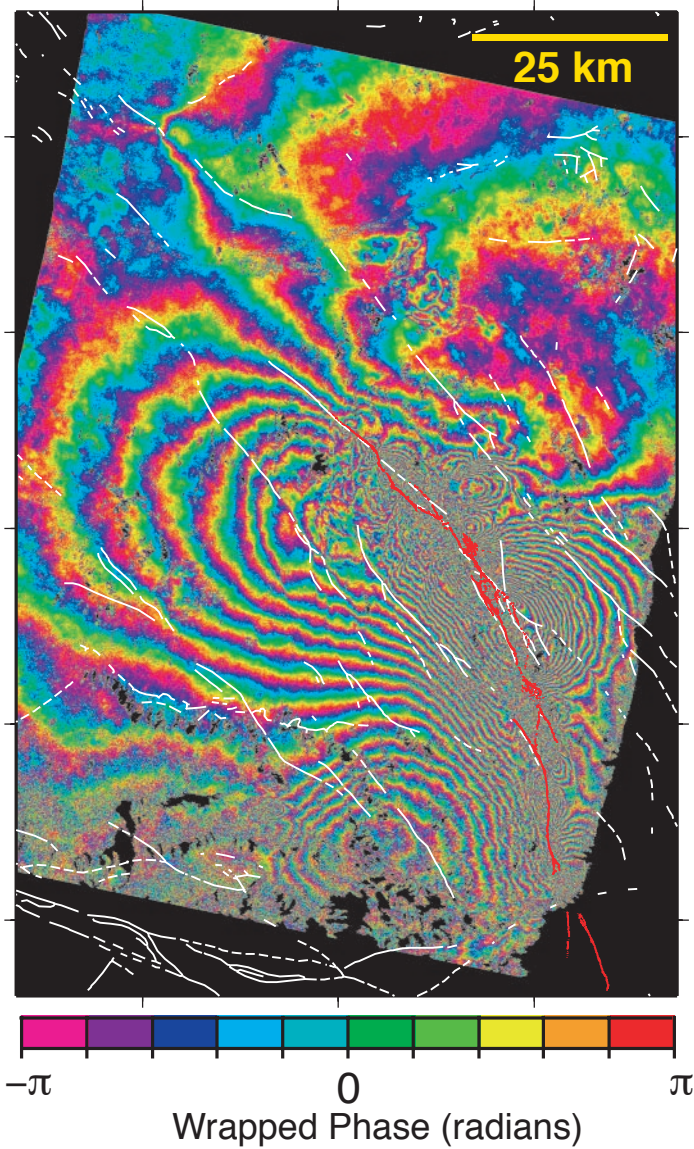


Figure 6 Landers coseismic deformation features from differential interferogram spanning 4/24/92–8/7/92 time period (modified from Price & Sandwell 1998). *Red lines* indicate the trace of the field mapped earthquake rupture, and *white lines* show other known faults in the region, some of which experienced triggered slip during the rupture sequence.

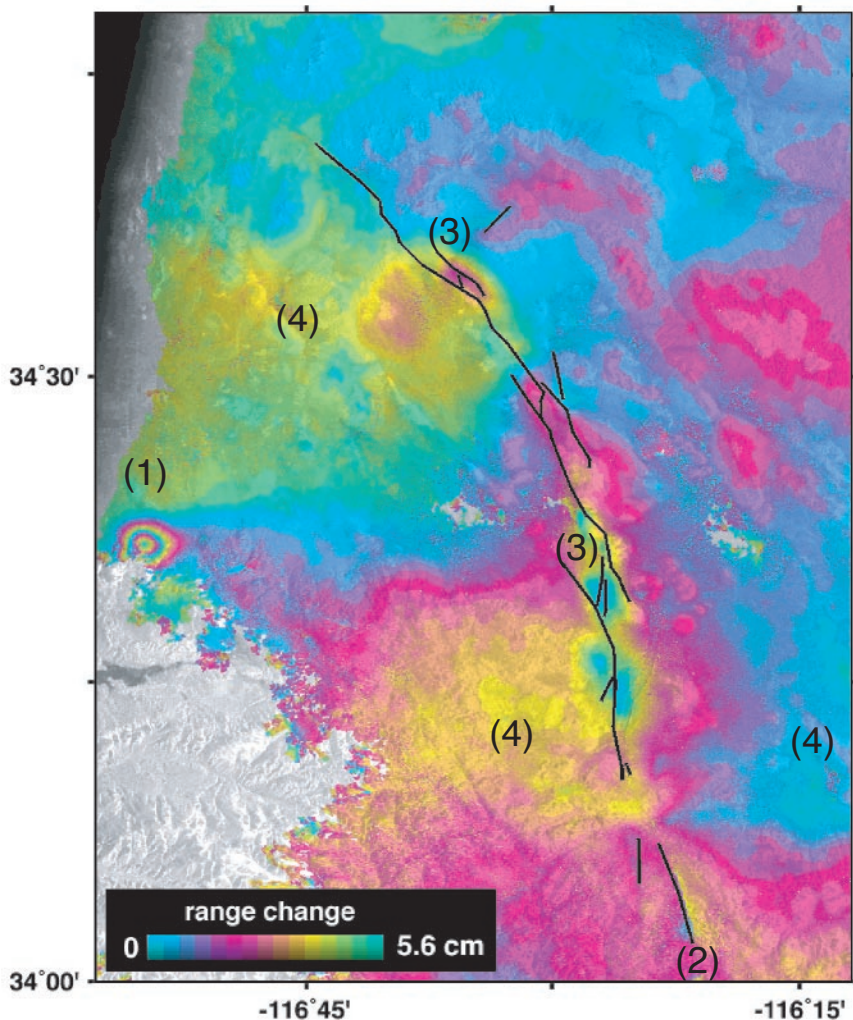


Figure 7 Interferogram of postseismic deformation following the 1992 Landers earthquake, covering the 09/27/92–01/23/96 time period (modified from Peltzer et al 1998b). The phase could not be unwrapped in the *gray areas* because of signal decorrelation over rough topography. *Black lines* indicate the coseismic surface rupture. The post-earthquake deformation includes (1) concentric fringes from the M=5.4 December 4, 1992 aftershock on *left* side of the image; (2) shallow afterslip along the Eureka Peak fault near *bottom* of image; (3) range decrease/increase in releasing/restraining step-overs of the coseismic rupture; and (4) broad antisymmetric range-change pattern about the rupture.

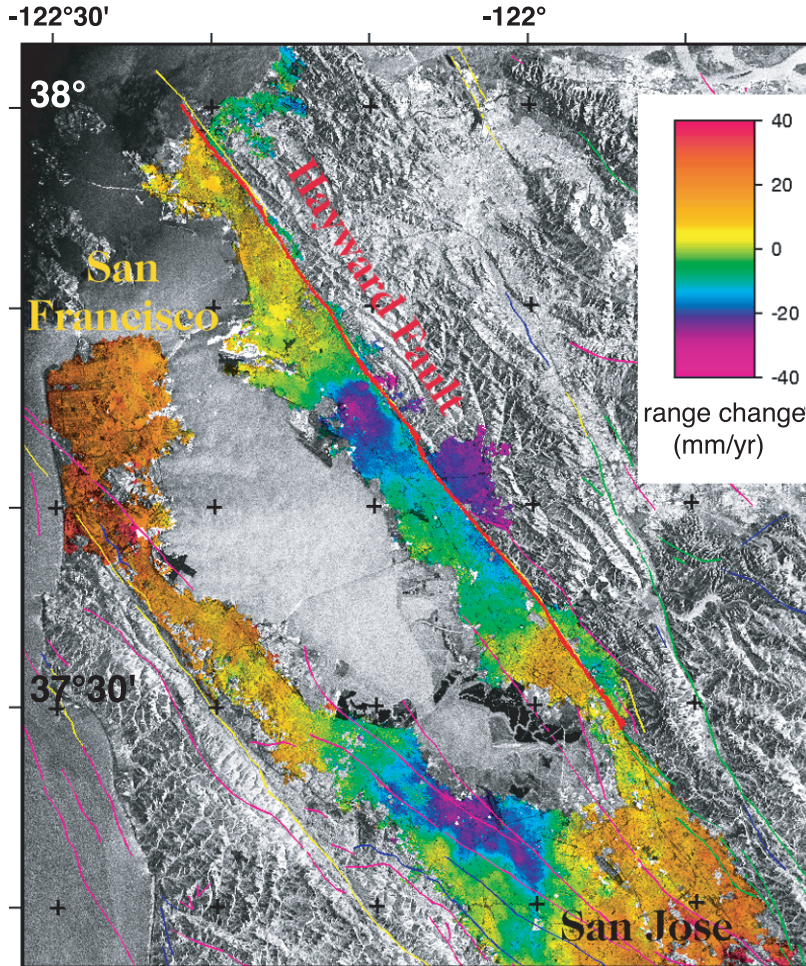


Figure 8 Unwrapped interferogram from two ERS-1 images acquired in June 1992 and September 1997 over the San Francisco Bay area, California. The radar amplitude is shown as a *grayscale* image, with the interferometric measurements rendered in color shades. Only the urbanized area could be mapped. Range changes across the Hayward fault (*bold red line*), represents 5–10 mm/yr of right-lateral slip during the 5 years between the two SAR images. The *blue* and *purple* areas near the bottom (Santa Clara Valley) and just west of the Hayward fault at 37°45' latitude moved upward by as much as 60 mm because of aquifer recharge during these wet years.

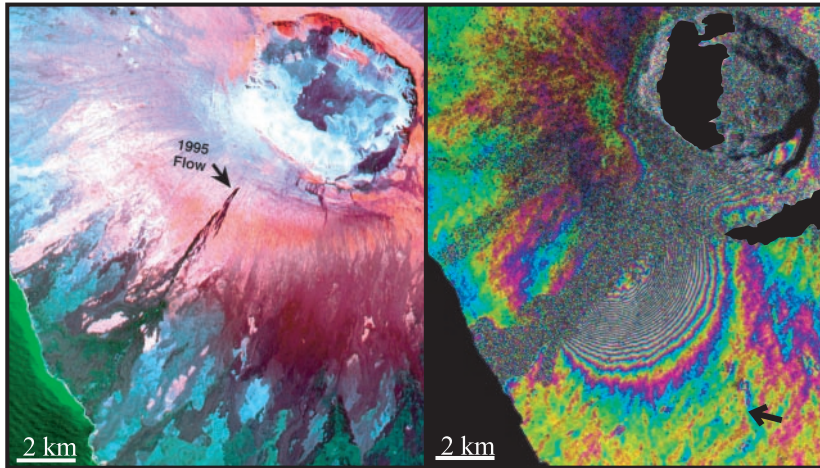


Figure 10 Radial dike intrusion and eruption on Fernandina Volcano, Galápagos, captured by an interferogram of images taken three years before and two years after the 1995 event (on *right*, modified from Jónsson et al 1999). The *arrow* shows the look direction of the ERS satellite down from the east. The strong decrease of the *semi-circular pattern* of range to the southeast of the active vent system suggests that the underlying feeder dike is dipping shallowly to the southeast, causing uplift above the intrusion. The false color SPOT image on the *left* shows the extent of the 1995 lava flow.

can be irregular, the resampling is usually done by spatial-domain interpolation techniques. Some care must be taken to design an interpolation filter that preserves the full spectral content of the image. After the second image is resampled, each complex pixel of the first image is multiplied by the complex conjugate of the same pixel in the second image. The interferogram then is a complex image itself, the phase of which is the difference of the signal phases that records the topography and the deformation accumulated between observation times. The amplitude of the interferogram is a measure of the cross-correlation of the images. This is the straightforward part of interferometry; with reasonably well-conditioned data, the process can be largely automated to this point.

The fourth step, the reduction of the interferogram's phase to a geophysical observable, is where expertise is required and where techniques diverge. As previously mentioned, to generate topographic maps, the phase must be unwrapped. There are dozens of papers on the subject, but none has solved the fundamental problem: Any consistent solution of the phase unwrapping problem—meaning any solution that is independent of integration path—is a possible realization of topography and deformation. Without independent information, such as from the radar image brightness or correlation, or from other sources such as a low-resolution DEM, there should be no expectation of error-free unwrapping. Still, for single-pass interferometric systems such as TOPSAR and SRTM, where the phase is relatively noise free and the geometry is favorable, phase unwrapping performance (by any method) is quite robust. For repeat-pass data, where temporal changes often obscure the phase measurement, phase unwrapping can be a challenge.

Reducing an interferogram to a deformation measurement requires removal of the topographic phase signature. This was originally done using a second interferogram with no expected deformation (Gabriel et al 1989). The phase of the topographic interferogram must be unwrapped, then scaled by the ratio of the baselines to match the phase rate of the interferogram encoding topography and deformation. This required unwrapping step is a hindrance. A more popular method uses a DEM as a topographic reference (Massonnet et al 1993). From orbit knowledge and the DEM, it is possible to simulate a topography-only interferogram and use this to remove the topography from the desired interferogram. This method avoids the unwrapping step for the topography but requires an existing DEM. In some cases, the use of the phase gradients can reduce the need for unwrapping (Price & Sandwell 1998). Obtaining the optimum results still requires some art, and different approaches and combinations of existing methods are being explored.

It is often desirable to unwrap the phase of the deformation signature to derive an absolute measure of line-of-sight motion across the interferogram. A continuous geodetic signal can be used directly in model inversions. An unambiguous record of deformation is an aid to the interpretation of new and subtle features. Unwrapping the deformation phase is often less difficult than the topographic

phase, because the deformation phase tends to vary more slowly. This is not always the case, however, for large events such as earthquakes or dike intrusions.

A final, extremely important step in obtaining the geophysical result is setting the absolute scale, or calibration. For both topography and deformation, the exact geometry is rarely known well enough for one to obtain the precise number of cycles of phase difference between observations. Interferometry tends to be a relative measurement. Most reports of deformation in the literature usually assume that the phase away from the area of study is zero. This is a reasonable assumption for localized signals such as volcanic caldera inflation. However, if the deformation to be measured varies broadly across the full image, as is the case for the broadly distributed strain field across a plate boundary, this assumption is not valid. In such cases, it is valuable to have point measurements from GPS provide independent tie points (Peltzer et al 1998a).

INTERFEROMETRIC CHARACTERISTICS AND LIMITATIONS

As radar interferometry has matured, a deeper understanding of its strengths and limitations has arisen. In particular, it is now recognized that those working in the field must cope with a number of important inherent properties of interferometry data, and with particular problems associated with existing systems, to avoid misinterpretation of the measurements. These properties generally fall into three categories: phase noise introduced by a variety of sources associated with the radar and wave propagation and scattering physics; height noise introduced in the mapping process by uncertainties in the dimensions of the interferometer; and geometric distortion associated with radar imaging. Some of these characteristics and limitations are inherent to radar and interferometry and can be dealt with only by specific manipulations of data products. Others can be reduced by improved system design. Table 1 summarizes these effects. The intent of this section is to touch on each of the limitations, giving the reader an indication of how to approach the radar data but relying on the literature to provide the details.

Phase Errors

Phase noise in interferometry is introduced in the radar system, in the propagation path through the variably refractive atmosphere, in spatial decorrelation of the electromagnetic fields scattered back from the surface elements, and in processing. These noise sources generate randomness in the interferometric phase, which, as we have seen, translates into height errors in topographic maps and displacement errors in deformation maps.

As identified in Table 1, some of these noise terms randomly change from pixel to pixel, some slowly and systematically change in space or time, and others depend on the nature of the data.

TABLE 1 Errors of InSAR measurements

Category	Character	Type	Origin
Phase errors	Random broad-band, characterized by interferometric correlation	Thermal noise	Radar system
		Quantization noise	
		Ambiguity/sidelobenoise (multiplicative)	
		Baseline decorrelation	Electromagnetic field correlations
		Volumetric decorrelation	
	Slowly varying systematic	Temporal decorrelation	
		Misregistration noise	Processor
		Number noise	
		Receiver phase instabilities	Radar system
		Atmosphere	Propagation path
Data dependent, systematic and/or random	Ionosphere		
	Phase unwrapping errors	Processing	
	Source DEM errors	Differential processing	
Metrology errors	Generally systematic, can be random if platform motion is severe and uncompensated	Baseline error	System geometry uncertainty
		Platform position error	
		Range error	
Data gaps	Terrain dependent	Layover	Image distortion
		Shadow	

Interferometric Correlation For random processes, the standard measure of the degree of statistical similarity of two signals forming an interferometric measurement is the correlation defined as

$$\gamma = \frac{|\langle c_1 c_2^* \rangle|}{\sqrt{\langle c_1 c_1^* \rangle \langle c_2 c_2^* \rangle}}, \quad (4)$$

where c_i is the image phase measurement at antenna i , and $\langle \rangle$ denotes ensemble averaging. Note that $\langle c_1 c_2^* \rangle$ is the interferogram, the phase of which captures the topography and deformation. Thus, the statistics of the interferometric phase are derived from the probability density functions of the interferogram and are parameterized by the correlation γ , which is the normalized modulus of the interferogram. Several papers have derived the statistics and distributions of interferograms (Lee et al 1992, Joughin et al 1994) and the relationship between

γ and phase (Rodriguez & Martin 1992, Zebker & Villasenor 1992, Bamler & Hartl 1998).

The expectation $\langle \rangle$ is usually approximated by area averaging. For a scene with uniform statistics, the maximum likelihood estimators of the interferometric phase and correlation are given by

$$\hat{\phi} = \arg \sum_{i=1}^{i=N} \sum_{j=1}^{j=M} c_1(i, j)c_2^*(i, j)/NM, \quad (5)$$

$$\hat{\gamma} = \frac{\left| \sum_{i=1}^{i=N} \sum_{j=1}^{j=M} c_1(i, j)c_2^*(i, j) \right|}{\sum_{i=1}^{i=N} \sum_{j=1}^{j=M} c_1(i, j)c_2^*(i, j) \sum_{i=1}^{i=N} \sum_{j=1}^{j=M} c_1(i, j)c_2^*(i, j)}. \quad (6)$$

For low correlation areas and when the number of points in the average is small, the correlation tends to be overestimated by this method. For example, if $N = 1$ and $M = 1$ in Equation 6, $\hat{\gamma} = 1$. The estimate can also be biased downward by a high rate of phase change over the averaging window. It is best to remove this local phase ramp prior to estimation.

The relationship between the correlation and the phase variance was explored by Zebker & Villasenor (1992). Rodriguez & Martin (1992) derived a lower bound on the phase variance in terms of the correlation

$$\sigma_{\phi}^2 = \frac{1}{2NM} \frac{1 - \gamma^2}{\gamma^2}, \quad (7)$$

which is a fairly good approximation to the exact relationship when $NM \geq \sim 4$. Note that since $\hat{\gamma}$ often overestimates γ for low correlation areas, its use in the above equation will tend to underestimate the phase variance. In a practical sense, one can form a correlation map from the data and use Equation 7 to quantify the phase and height or deformation errors. In this sense, interferometry is a quantitative tool with known statistical accuracy.

Statistical Errors Statistical phase noise is introduced in the receiver as thermal and quantization noise; this is effected by statistical differences in the scattering geometries of the two interferometric observations, first characterized for InSAR by Zebker & Villasenor (1992), and by number precision limits in processing.

Thermal noise is introduced because a radar operates at a non-zero temperature and observes warm objects, which excites thermal motions of electrons in the radar system. Generally, thermal noise is uncorrelated with the return echo. Decorrelation introduced by thermal noise can be minimized by increasing the transmitted signal power.

Misregistration of the images forming the interferogram also introduces random noise because partially incommensurate random signals from neighboring pixels are mixed in forming the interferogram. When orbits are known to a small fraction ($1/20$) of a pixel, this error is negligible. When orbits are poorly known and the registration offsets must be estimated from the data, the error becomes a function of the intrinsic field correlation.

Quantization noise arises in modern radars that sample the continuous received waveforms and digitize the signals. The digitization process quantizes the received voltages, introducing a random component similar to thermal noise. If the signal level is very dynamic, it is also possible that the signal will be lost when it is too low, or saturated when it is too high. Generally, radars are designed with a sufficient number of bits to keep the quantization noise at a low level.

Number noise is added in interferometric processing because computers have finite word lengths. This is usually very small and can be neglected.

Several noise terms are introduced by electromagnetic field correlations. If an image point is viewed from a slightly different angle in the two images, the contributions from scatterers within the pixel area add up differently. From a purely geometric point of view, the path lengths from the radar to the individual scatterers are slightly different at the two viewpoints. Because radar is a coherent imaging method, the randomly arranged set of scatterers will give a randomly different signal. This leads to a decrease in correlation with increasing baseline; this is called geometric or baseline decorrelation. The topographic fringe frequency is proportional to the range-perpendicular component of the baseline. If the phase change across an element is 2π or more, due to topographic slope, differential surface motion, or large antenna baseline, the interferometric signal decorrelates and does not allow for the creation of an interferogram. For topographic applications, we seek the maximum spatial baseline with acceptable geometric decorrelation. For deformation applications, we seek the smallest possible spatial baseline, thus minimizing topographic effects and geometric decorrelation. When vegetation or extremely rough surfaces are present in a pixel, the concept of baseline decorrelation can be extended to the pixel volume (Rodriguez & Martin 1992). In this case, the signal decorrelates at a faster rate as the baseline increases because the effective range-perpendicular resolution is larger.

Any temporal change within the target scene (such as vegetation growth or movement, erosion, cultivation, and so on) may cause decorrelation between the two imaging passes used in an interferogram (Zebker & Villasenor 1992). Choice of the appropriate temporal baseline for an interferogram depends on the application (milliseconds to seconds for ocean currents, days for glacial flow, and up to several years for crustal deformation studies). Over regions dominated by bare

bedrock—such as deserts or unvegetated volcanoes—and over urban areas, interferometric image pairs can successfully span many years (full 7-year duration of the ongoing ERS mission). The wavelength of the radar also can affect temporal decorrelation: The 5.6-cm C-band has high fringe rates and decorrelates relatively easily even in lightly vegetated areas, whereas the 24-cm L-band often penetrates through surficial vegetation and is more reliable in mountainous areas as well (Massonnet et al 1996a, Rosen et al 1996, Zebker et al 1997).

Radar ambiguities and sidelobes of the impulse response (Curlander & McDonough 1991) are by definition dependent on scene brightness variations. A radar ambiguity is a ghost of a feature that appears elsewhere in the image at reduced brightness. Ambiguities affect interferometry by introducing a brightness-dependent phase term to the interferometric phase away from that feature. An ambiguity from a bright feature that appears in a dark region can significantly alter the phase. It is difficult to quantify the effects of ambiguities a priori; however, the correlation estimate captures it. Some ambiguities and side-lobe effects can be reduced in the radar processing by sacrificing resolution.

Systematic Errors For systematic errors, the interferometric phase changes vary little between neighboring pixels. These errors include slow phase instabilities in the radar receiver chain (Rosen et al 2000) and propagation effects and are typically characterized by their characteristic time (or distance) scales (Goldstein 1995, Fujiwara et al 1998a). The velocity of wave propagation between a satellite and the surface of the Earth is affected by the composition of the atmosphere. Thus, an additional phase term results from atmospheric heterogeneity. For systems with dual antennas measuring topography, such as SRTM, the difference in phase between the two observations induced by the atmosphere is quite small and can be ignored for all but the most accurate (submeter) mapping systems. For repeat-track observations, this noise source can often be the limiting effect. Particularly large offsets can result from water in the troposphere. A change in humidity of 20% can result in a phase delay corresponding to a 10-cm error in deformation measurements and topographic errors exceeding 100 m (Goldstein 1995, Rosen et al 1996, Tarayre & Massonnet 1996, Zebker et al 1997). Figure 3 shows an example of a systematic range change bias introduced by the differential delays across a mountain divide between moist windward air masses and dryer air in the rain shadow, on the Izu Peninsula, Japan (Fujiwara et al 1998a).

To minimize atmospheric disturbances in interferograms, researchers can identify particular scenes that have large atmospheric artifacts and not include those data in their deformation analysis (Massonnet et al 1994). Atmospheric effects can also be reduced by averaging a large number of interferograms where uncorrelated atmospheric delays cancel out (Zebker et al 1997, Fujiwara et al 1998a, Sandwell & Price 1998). In some situations, it might be possible to produce and subtract a model of atmospheric delays from complementary observations made with GPS or other atmospheric sensors (Delacourt et al 1998, Williams et al 1998).

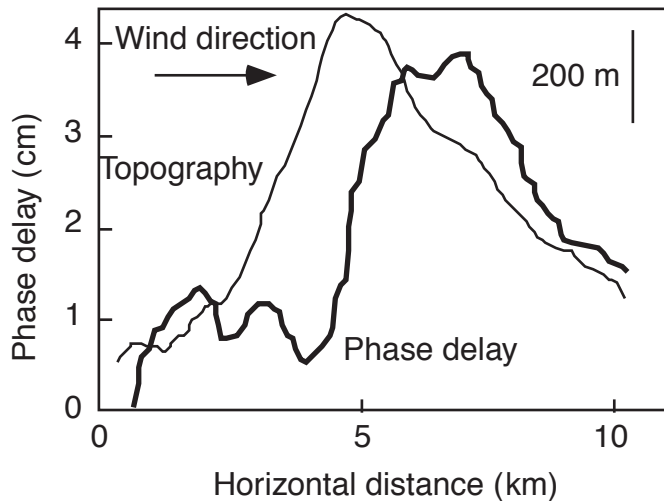


Figure 3 Cross section of the phase delay (*bold line*) and topography (*thin line*) along a west-to-east profile across the western Izu Peninsula, Japan. When the first of the images (from 8/20/93–11/16/93) used in the JERS-1 interferogram was taken, it rained on the windward side, but little precipitation occurred to the east. Apparently the rising air on the western flank of the mountains and dry air on the eastern flank produced a systematic bias in the range change pattern that easily could be mistaken as a deformation feature (modified from Fujiwara et al 1998a).

For topographic applications it is advantageous to maximize the perpendicular baseline to minimize this problem.

Data-Dependent Errors Other phase noise sources are data or processing dependent. A variety of phase unwrapping methods exist, each with data-dependent noise characteristics (Bamler et al 1998, Ghiglia & Pritt 1998). Some algorithms introduce phase errors in integer multiples of 2π (Goldstein et al 1988) whereas others produce distortions to the phase field radiating from a phase anomaly (Ghiglia & Romero 1989). It can be difficult to predict the location of these errors in noisy data without knowledge of the topography. Most repeat-track data for deformation studies are noisy over some part of the image. This is an area of interferometry where examining several datasets, perhaps acquired at slightly different times or with different sensors and viewing geometry, can be extremely helpful.

In processing for deformation studies, the DEM used to remove topography from an interferogram can introduce errors. Whether the DEM is generated interferometrically [the three-pass method (Gabriel & Goldstein 1988)] or acquired from an independent source [the so-called two-pass method (Massonnet et al 1993)], topographic errors in the DEM will lead to errors in the deformation map.

A height error Δh in the DEM will lead to a phase error of $\Delta h/h_0$ in fringe cycles, which can be scaled to meters by the radar wavelength to give the deformation error introduced by topographic errors.

Metrology Errors

For topographic applications, or for removing the topography from a deformation interferogram, accurate knowledge of the geometry of the interferometric triangle formed by the baseline \vec{B} and the ranges ρ_1 and ρ_2 is essential, usually at the scale of several millimeters for the baseline. Airborne topographic mapping interferometers are usually designed to meet a particular map accuracy specification, and measurement devices such as inertial navigation units, GPS receivers, and baseline metrology systems are configured into the system. SRTM also has similar devices. Repeat pass systems can rarely determine the orbit, and hence the baseline, to this accuracy; therefore, ground control points are used to estimate the baseline and the absolute phase constant. The final absolute map accuracy is thus a function of the accuracy of the ground control points.

Data Gaps

Depending on the topographic slope and look angle, some portions of a mountainous region may not be visible because they are located in the shadow of the illuminating radar. Clearly, it will not be possible to make interferometric measurements of those areas. If the topographic slope in the direction toward the radar exceeds the radar incidence angle, then at least two points will have the same range distance to the radar (so-called layover) and therefore will not be separable in the SAR image. For example, a mountain would be mapped to the same image point as some point in a nearby valley located at the same distance from the radar. Steep slopes that are close to the radar incidence angle will also have interferometric decorrelation, even if they are not in true layover.

Other Limitations

Interferometry approaches its limits of utility as the phase changes by more than one cycle from one image pixel to the next. For topography measurements, this implies that the geometric decorrelation is very high, so the data will be very noisy. For crustal deformation measurements, it implies that the rate of the deforming process exceeds the spatial sampling rate of the data (Massonnet & Feigl 1998). This is a limitation on monitoring both large displacement gradients and rotations (Zebker & Villasenor 1992). It is an inherent limitation of a particular system, but in many cases systems with finer spatial or temporal resolution, or with longer wavelengths, can be employed to reduce the problem.

A final inherent limitation of radar interferometry for deformation is that the motions are measured only in range direction; thus, scalar, not vector, deformation measurements are possible. Although InSAR has good sensitivity to vertical dis-

placements, particularly for sensors such as ERS where the look angle varies from 20.5° to 25.9° across an image, it is insensitive to motions parallel to the satellite track. This limitation can again be reduced through combinations of data taken from different look directions (Massonnet et al 1996a).

Summary of Limitations

With so many error sources, one might get the impression that the errors and limitations in interferometry far outweigh the measurements. Indeed, at times the decorrelation can be so great that a scene cannot be used, or mountains so high that the region of interest is hidden in shadows. But for the vast majority of data, these effects are identifiable through the correlation map and a little knowledge about the area of interest. The least controllable aspects of interferometry with a given sensor are temporal decorrelation and systematic phase errors introduced by propagation effects or phase unwrapping algorithms. With the currently limited availability of data, there are occasions when detailed analysis beyond the interferogram is not possible. But with the increasing quantities of available data in the future, these limitations will undoubtedly be reduced dramatically, just as continuous GPS allows for much improved reduction of errors in displacement measurements through long-time integrations.

INSAR STUDIES OF EARTH'S TOPOGRAPHY

The surface of a planet is shaped by the interaction of constructional and erosional processes over geologic timescales. Quantification of the surface morphology is the first step to understanding these processes. The accumulation of tectonic strain deforms the surface, and volcanic processes both construct edifices and rapidly deform them. On the Earth, water (liquid or as ice) is an effective erosional medium in nearly all environments, wearing away topographic features with the help of mass wasting in steeper terrain. Erosion rates generally depend strongly on the local slope angles, and river drainage networks are controlled by topography, so quantification of the surface shape is essential. Topography is also important in many human activities, from building transportation infrastructure to mitigating floods and landslides.

Generation of DEMs Before InSAR

Topographic maps have a long history, starting with qualitative expressions of hills, valleys, and mountains on general maps and continuing with quantitative topographic contour maps. The advent of stereo aerial photography in the first part of the twentieth century made possible photogrammetric measurements of elevations over substantial areas, and many regions have been mapped at various scales by these means. Stereo images or photographs taken by satellites are also used to construct topographic maps, and most of the earth's land surface has been

mapped at least at 1:1,000,000 scale [e.g. Operational Navigation Charts (ONC) of the US National Imaging and Mapping Agency]. A major problem for optical imagery in some areas is cloud cover that prevents imaging of the ground surface from space; the lack of contrasting features prevents stereomatching in other areas, especially on ice sheets. Although stereo radar imagery, especially from the Radarsat system, has been used for stereogrammetric generation of DEMs, nearly all stereogrammetry is done with optical images.

The first digital elevation models (DEMs) were made by digitizing contours from topographic maps and interpolating the elevations to form a regular grid. This technique is still used in some areas where high-quality topographic contour maps are available. Most of the 3-arcsecond (~ 90 -m) DEMs for the United States, distributed by the US Geological Survey (online at EROS Data Center) were interpolated from contours digitized on 1:250,000 maps (USGS 1993). Some parts of the recently produced global DEM GTOPO30 (<http://edcwww.cr.usgs.gov/landdaac/gtopo30/gtopo30.html>), which has a 30-arcsecond grid spacing, were interpolated from the contours of the 1:1,000,000 ONC charts.

Unique Capabilities of InSAR in Studies of Earth's Topography

As described previously, both repeat-pass SAR interferometry and simultaneous interferometric systems are now used to produce DEMs. Similar to optical stereogrammetry, airplane SAR systems produce higher resolution data than do satellite platforms because they are closer to the ground (note the distance to the ground ρ_1 in Equation 1, which is usually a factor of 20 larger for satellites than for airplanes). Processing of airborne SAR is more difficult because the irregular motions of the airplane must be compensated for precise imaging and interferometry (Zebker et al 1992, Madsen et al 1995). The chief advantages of InSAR over optical stereogrammetry are few or no requirements for manual selection of ground control points, capability to measure elevations over featureless areas, and imaging through clouds and darkness. Space-based InSAR does not provide the only means to produce high-quality DEMs of the Earth's surface, but it can do so globally and in an especially timely and reliable fashion.

Simultaneous interferometric systems, where the two SAR images are acquired simultaneously by dual radar antennas, have many advantages for DEM generation over systems that acquire SAR images at different times. Because the two radar antennas are usually attached to the same platform, the length and orientation of the interferometric baseline (\vec{B} in Equation 1) is much easier to measure than for repeat-pass systems. In addition, the planetary surface cannot change between the two radar images, so the interferometric correlation is extremely high, even with short radar wavelengths, and there is no surface deformation signal for simultaneous systems.

Many spaceborne SAR systems produce repeat-pass interferometry that might be used for DEM generation. Two mission phases were specifically designed to

optimize the acquisition of data for generating DEMs by shortening the time interval between the SAR images. During the last few days of SRL-2 (Spaceborne Radar Laboratory flight 2) in October 1994, the Space Shuttle orbit was modified to repeat orbits once a day. The SIR-C and X-SAR instruments collected high-resolution interferometric data at L-, C-, and X-band wavelengths during these orbits over widely spaced locations. In April 1995, the ERS-2 satellite was launched into an orbit that repeated the same orbits as the continuing ERS-1 satellite on the following day. This tandem ERS-1/ERS-2 mission phase collected a large number of C-band interferometric pairs with a 1-day separation over most of the earth's land surface between May 1995 and June 1996, plus some tandem pairs after that intensive acquisition period.

As we discuss in the section on errors, atmospheric changes between the times of two SAR images in an interferometric pair can affect the measured phase. This is a significant problem for repeat-pass interferometric DEMs, but it can be reduced in some cases by finding an image pair that has little atmospheric change. SAR images acquired during the night (e.g. ascending ERS scenes) generally have calmer atmospheric conditions (Massonnet & Feigl 1998). The atmosphere also contains more water at lower elevations and higher temperatures, so tropical lowlands are more likely to have atmospheric problems than cold, high-altitude areas (Zebker et al 1997). Decorrelation over heavily vegetated areas, especially at the shorter C-band wavelength, also prevents the application of repeat-pass interferometry in some regions.

Applications of InSAR in Topographic Studies

As with many new techniques, most of the early InSAR topographic acquisitions have been designed to test the development of the systems and then calibrate and verify the results. The airborne TOPSAR system, operated primarily for NASA investigators, has produced DEMs in a variety of environments starting with early configurations in 1991 (Zebker et al 1992, Mouginiis-Mark & Garbeil 1993, Lin et al 1994, Madsen et al 1995). Several large TOPSAR mosaics have been acquired over geologic targets, from volcanoes and calderas to actively uplifting mountains and fault zones.

Active basaltic shield volcanoes are among the cleanest examples of constructional morphology. Mouginiis-Mark et al (1996) and Rowland (1996) studied the morphology of the Galapagos Islands, especially Isla Fernandina, with TOPSAR DEMs and several types of satellite imagery. A DEM mosaic of five TOPSAR swaths for Fernandina, acquired in 1993, was used to produce several products, including shaded relief and slope maps (Figure 4, color insert) that clearly show the major morphologic zones of the single-volcano island. Rowland (1996) used the detailed TOPSAR mosaic as a planimetric base to combine optical imagery from SPOT and Landsat TM with SIR-C radar imagery and made a geologic map of the volcanic flows and their source vents. He then used the TOPSAR data to estimate the thickness and volumes of the flows, separated into two age classes,

to conclude that the lava effusion rates have changed significantly. The interferometrically measured TOPSAR DEM was the key to all these results.

Stratovolcanoes and orogenic belts with active uplift and erosion often have steep slopes that limit the usability of interferometric SAR with steep (near-vertical) incidence angles such as ERS. In addition, many mountains have zones of heavy vegetation that frustrate the application of C-band repeat-pass interferometry. The SIR-C exact-repeat experiment yielded tantalizing samples of data similar to what will be acquired by SRTM. The L-band wavelength on SIR-C provided high coherence, and the adjustable incidence angle allowed imaging of steeper slopes with shallow incidence angles that avoid layover. Coltelli et al (1996) used the SIR-C/X-SAR mission to produce a DEM for the stratovolcano Mt. Etna. They took advantage of the multiple wavelengths collected simultaneously to aid in the phase unwrapping step and reduce the height errors. Supervised classification of the interferometric coherence at the three radar wavelengths (X-, C-, and L-band) was used to map different volcanic terrains. MacKay et al (1998) made a SIR-C DEM of Karisimbi volcano in Rwanda and were able to map the thicknesses and volumes of massive trachyte lava flows. These flows average 40–60 m in thickness, and surface features visible in the DEM allow estimates of the apparent lava viscosity (MacKay et al 1998). For additional information on InSAR studies of the morphology of active volcanoes, see also Francis (1999) and Zebker et al (1999).

A SIR-C DEM over part of the Altyn Tagh fault in the Kun Lun Mountains at the northern edge of Tibet is shown in a perspective view in Figure 5 (see color insert; Fielding 1999). The active strand of the fault runs up the north side of the valley in this section. Just above the left-lateral fault are many faceted spurs, and below it are uplifted fan surfaces. The narrow 25-km swath of SIR-C interferometry limits the coverage of this major tectonic feature, but the DEM shows the potential of interferometric DEMs for tectonic geomorphology. SRTM will produce a global DEM with slightly coarser resolution than this example.

INSAR STUDIES OF CRUSTAL DEFORMATION

Until the advent of space geodesy, measurements of surface motions relied on terrestrial methods of which triangulation, trilateration, and spirit leveling were the most commonly used. In these geodetic methods, surveyors repeatedly measure horizontal angles, distances, or elevation differences between a number of benchmarks set in the ground. Changes of these measurements with time indicate deformation of the crust. These data proved invaluable in developing and improving our understanding of the mechanics of the earthquake cycle and of active deformation in many plate boundary zones, on volcanoes, and in areas affected by land subsidence. Terrestrial methods provide precise measurements of deformation; however, they are time intensive and costly, are restricted to sparse point

measurements, and do not allow for the direct measurement of three-dimensional displacements.

Unlike terrestrial methods, space geodetic methods do not require line of sight between stations in a network, and they do not rely on good weather and daylight; also, errors in the measurements accumulate much more slowly with increasing distances between stations. Space geodetic methods rely on measurements of signals from extraterrestrial objects or earth-orbiting satellites. Very long baseline interferometry (VLBI), satellite laser ranging (SLR), and the global positioning system (GPS) made studies of motions on a global scale possible. For the last decade, GPS has been the tool of choice for studies of deformation along active plate boundaries, plate tectonic motions, and deformation on volcanoes (e.g. Segall & Davis 1997). The principal of GPS geodesy is based on measuring the range to several GPS satellites from the time it takes for a signal to be transmitted from the satellites at $\sim 20,000$ -km altitude to a receiver (e.g. Dixon 1991, Hager et al 1991, Segall & Davis 1997). GPS provides all three components of surface displacements in an external reference frame, which is not possible with the terrestrial methods or with InSAR. Precision of the horizontal component measurements is 2–5 mm, whereas the vertical component is two to three times less precise. Many of the recent breakthrough technologies for active deformation studies were developed for other scientific or applied purposes, such as radio astronomy (VLBI), military navigation (GPS), and remote sensing and topographic mapping (SAR). Synthetic aperture radar (SAR) interferometry is only the latest and potentially most exciting inadvertent addition to the space-geodetic arsenal of earth scientists studying crustal deformation.

InSAR brings some unique capabilities to the toolbox of crustal deformation researchers; these capabilities allow for the study of active processes that are inaccessible with the traditional methods. Although the deformation measurement capabilities of InSAR had been demonstrated earlier (Gabriel et al 1989), it was the successful measurement of deformation associated with the 1992 Landers earthquake that demonstrated the revolutionary nature of the technique. Using interferometric images of ERS-1 satellite radar data collected before and after the Landers earthquake, scientists were able to image the deformation surrounding the rupture in astounding detail (Massonnet et al 1993, Zebker et al 1994).

However, it was found that the coseismic displacements of GPS stations in the epicentral region, as well as field observations of the surface ground deformation and inversions of seismic data, allowed for comparable resolution of earthquake slip, as did the interferograms. What, then, are the outstanding characteristics of InSAR that are not realistically achieved with other techniques, and which primary applications will benefit from these features? First, InSAR maps surface deformation at dense pixel spacing of 20–100 m over almost unlimited spatial distances. Second, InSAR is particularly sensitive to vertical displacements comparable to the precision of leveling measurements. And last, InSAR distinguishes itself from all other precise geodetic techniques in that it is a remote-sensing tool that requires no presence in the field and is available practically worldwide. Of

course, in our preceding section on errors and limitations we discuss a number of severe practical limitations that handicap InSAR in some situations.

Nonetheless, the breakthrough applications we see for InSAR in the study of deformation at the Earth's surface consequently fall into three categories: (a) surface deformation processes that vary in a complex fashion over short distances but are distributed over wide areas (these include shallow active faulting associated with complex earthquake ruptures, surface creep, triggered slip and after-shock activity, volcanic processes, and details of surface motions related to subsurface movement of fluids); (b) deformation that is dominated by complex vertical motions such as can be found above geothermal systems and volcanoes, and areas affected by land subsidence; (c) measurement of deformation events in remote, dangerous, and inaccessible areas. These include response to and characterization of earthquakes and volcanic eruptions in regions devoid of any other geodetic monitoring activities, or where access might be hazardous to field personnel.

In this section, we review applications of InSAR in crustal deformation research, highlighting a number of studies that exemplify the unique utility of InSAR. We hope that these examples give a good representation of the capabilities of the technique and the foreseeable advances in future research of the earthquake cycle, volcanic deformation, and subsurface fluid transport.

Earthquake Deformation

It is notable, but perhaps not surprising, that the number of earthquakes investigated with InSAR is quickly approaching the number of earthquakes studied with GPS during the last decade. These include investigations of the 1992 Landers, California, earthquake (Massonnet et al 1993, Peltzer et al 1994, Zebker et al 1994, Price & Sandwell 1998) and its aftershocks (Massonnet et al 1994, Feigl et al 1995); the 1993 Eureka Valley, Nevada, earthquake (Massonnet & Feigl 1995b, Peltzer & Rosen 1995); the 1994 Northridge, California, earthquake (Massonnet et al 1996a, Murakami et al 1996); the 1995 Kobe, Japan, earthquake (Ozawa et al 1997); the 1995 Grevena, Greece, earthquake (Meyer et al 1996); the 1995 North Sakhalin Island, Russia, earthquake (Tobita et al 1998); the 1995 Antofagasta earthquake (Pritchard et al 1998); the 1995 Dinar, Turkey, earthquake (Wright et al 1999); and the 1997 Kagoshima-Kenhokuseibu, Japan, earthquake (Fujiwara et al 1998b).

Radar interferometry does not depend on field surveys of benchmark locations before an earthquake. Thus, if a prior image has been acquired and archived, and if a coherent interferogram can be produced with a post-earthquake image, it is possible to study the coseismic deformation of an event even in the most remote regions of the world. Because GPS measurements are usually spaced tens of kilometers apart, they are unlikely to capture smaller events or details of a larger rupture. InSAR, on the other hand, has imaged shallow events of small magnitude that only deformed an area of a few square kilometers. In this section we review a few representative applications of InSAR to earthquake studies, many drawn

from studies related to the 1992 Landers sequence. The Landers earthquake and its aftermath imaged with the ERS sensor exemplifies the unique capabilities InSAR contributes to crustal deformation studies. We do not strive to provide a comprehensive review of all InSAR studies of tectonic deformation but hope to give an overview of the capabilities of the method that may lead to significant improvements in our understanding of the physics of the earthquake cycle.

The June 28, 1992, Landers earthquake was the first tectonic event captured and studied in detail with InSAR (Massonnet et al 1993, Massonnet et al 1994, Peltzer et al 1994, Zebker et al 1994, Massonnet & Feigl 1995a, Hernandez et al 1997, Price & Sandwell 1998). This $M = 7.3$ strike-slip event ruptured an ~ 85 -km-long series of fault segments in the Mojave Desert of California. It was soon followed by the $M = 6.2$ Big Bear event that broke a left-lateral fault perpendicular to and southwest of the Landers rupture. Although the broad deformation field of the event was well captured by conventional GPS measurements, the InSAR imagery provided a wealth of information about small-scale deformation processes in the near and far fields of the event. Furthermore, InSAR data proved particularly valuable in the investigation of post-earthquake deformation patterns, as detailed below.

The coseismic interferogram recorded over 50 cm of range change caused by lateral motions away from and toward the ERS spacecraft, as well as vertical displacements in areas of contraction and extension surrounding the rupture (Figure 6, color insert). The observations are well explained by dislocation models of several meters of strike slip in the upper 10 km of an elastic half-space. The coseismic rupture in this relatively well-monitored region was adequately characterized by traditional geodetic and seismologic techniques (Murray et al 1993, Cohee & Beroza 1994, Freymueller et al 1994, Hudnut et al 1994, Wald & Heaton 1994); however, the InSAR data captured deformation of much more localized nature that is not apparent in the other data sets. Peltzer et al (1994) examine fine details of the deformation field in the vicinity of the fault trace. They identify range change patterns that are consistent with block tilting about a horizontal axis in a region located between two overlapping rupture segments. Along a 6-km-long fault segment that did not show any surface offsets in the field, Peltzer et al (1994) find dense fringe patterns, consistent with coseismic fault slip of several meters below 2 km that continues below the slip gap. Zebker et al (1994) note an area of distributed phase breaks that they interpret to be caused by extensive surface fracturing of a zone several kilometers wide, away from the main rupture.

In addition to the main coseismic rupture, several faults in the area experienced triggered slip of a few centimeters associated with the earthquake sequence. Massonnet et al (1994) and Price & Sandwell (1998) identify triggered slip on a large number of mapped faults within the broader vicinity of the rupture (Figure 6). Massonnet et al (1994) demonstrate that a ~ 20 -km-long segment of the left-lateral, east-west striking Garlock fault, located almost 100 km north of the rupture, slipped by about 2 cm. The InSAR studies also find evidence for slip on several subsidiary breaks that have not been identified on geologic maps. It is not

clear whether this induced slip is in response to small static stress changes or if it is a dynamic phenomenon that is related to the passage of seismic waves.

Postseismic Deformation

Of particular interest to scientists studying the earthquake cycle are transient processes that follow earthquakes in the days and years after a large event (e.g. Thatcher 1986, Shen et al 1994, Bürgmann et al 1997, Savage & Svarc 1997). Post-earthquake deformation includes aftershocks, afterslip on and surrounding the coseismic rupture, transient slip on nearby faults, and viscous relaxation of the mid-to-lower crust and upper mantle. Postseismic deformation can reveal valuable information about the rheology of the Earth's crust and the effect an earthquake has on neighboring faults. Postseismic deformation processes occur over a wide range of temporal and spatial scales, and InSAR is beginning to make important contributions to the study of several of these effects. If the wealth of information gleaned from the early postseismic period of the 1992 Landers earthquake is representative, InSAR is about to revolutionize our understanding of crustal deformation processes, fault interactions, and the rheology of the Earth's lithosphere.

Due to the high spatial resolution of InSAR, it has been possible to measure details of the deformation associated with an individual $M = 5.4$ aftershock of the Landers earthquake (Massonnet et al 1994, Feigl et al 1995) (Figure 7, color insert). Massonnet et al (1994, 1996b) analyzed several post-Landers-earthquake interferograms to deduce shallow surface slip immediately following the event on only a few rupture segments, afterslip on buried portions of the coseismic rupture, and suggestions of postseismic fault zone collapse. Peltzer et al (1998b) document details of the afterslip distribution on the Eureka Peak fault segment (Figure 7) of the Landers rupture consistent with an exponential decay with a relaxation time of 0.8 years. The total moment released in the afterslip of this segment is two orders of magnitude greater than that released by aftershocks in the vicinity of the Eureka Peak fault (Peltzer et al 1998b). Significant post-earthquake deformation has also been observed following the 1995 North Sakhalin Island, Russia, earthquake using the L-band JERS system (Tobita et al 1998).

A heretofore undocumented phenomenon, involving pore fluid flow in response to the coseismic stress change, can explain the post-earthquake deformation near fault segment step-overs imaged by InSAR (Peltzer et al 1996, Peltzer et al 1998b). Surprisingly, the postseismic InSAR data indicate subsidence in a restraining (left) step-over and uplift in releasing right steps of the rupture, opposite the coseismic motion and opposite that predicted if continued slip is the main post-earthquake deformation mechanism (Figure 7). Deformation due to fluid flow in response to pore-pressure changes provides a plausible mechanism that can produce this pattern (Peltzer et al 1996). Such a model, in combination with

afterslip on deeper portions of the coseismic rupture, is consistent with both GPS (Savage & Svarc 1997) and the InSAR data (Peltzer et al 1998b).

Stress changes induced by large earthquakes are expected to cause accelerated viscous flow of rocks located below the rupture. The predicted response is highly dependent on the effective viscosity of crustal and mantle rocks at elevated temperatures and pressures. Thus, observations of transient deformation in the years following an earthquake can provide direct constraints on some fundamental crustal rheology parameters. Continued stress changes from deep viscous relaxation may also affect the timing of future earthquakes even on rather distant faults. Deng et al (1998) and Pollitz et al (2000) integrate horizontal displacements measured with GPS and InSAR line-of-sight changes over several years to infer viscous deformation parameters of the lower crust and upper mantle. Usually, it is difficult to differentiate deformation patterns due to deep afterslip from viscous relaxation below long strike-slip ruptures (e.g. Thatcher 1983). The added information on vertical deformation surrounding the rupture provided by the InSAR data is not consistent with pure afterslip and allows for discrimination between different models of regional viscoelastic stratification (Pollitz et al 2000).

Interseismic Deformation

Plate boundary zones deform very slowly during much of the earthquake cycle when elastic strains steadily accumulate. Commonly, a few centimeters per year of displacement are distributed over a region tens of kilometers wide. Errors introduced by orbital and atmospheric effects and decorrelation over time have long spatial scales as well, so measuring broadly distributed deformation provides a great challenge to InSAR (Rosen et al 1998). Careful integration with GPS point measurements and better control of the above-mentioned error sources might allow for more successful InSAR investigations of interseismic strain fields in the future (Peltzer et al 1998a).

Of particular importance for earthquake hazard studies is the determination of the contribution of aseismic deformation to the slip budget along major faults. Several major faults of the San Andreas fault system apparently accommodate a significant portion of their slip budget by aseismic creep, including the central San Andreas fault and the Hayward and Calaveras faults. However, these faults have also experienced large earthquake ruptures, and we need to better understand the detailed distribution of locked and creeping patches to improve our earthquake potential estimates. Measurements of surface displacements surrounding a fault can be used to compute models of the distribution of slip on a fault system (Harris & Segall 1987). To successfully resolve details of the slip distribution along such a complex fault zone, we require closely spaced measurements around the fault. Current geodetic networks with GPS sites spaced at approximately 10-km intervals do not allow us to deduce such detailed slip patterns. InSAR, with its order-

of-magnitude improved measurement-point spacing, promises to significantly enhance such studies.

Along several faults of the San Andreas system that aseismically slip near the surface, discrete offsets are apparent in interferograms spanning extended time periods (Bürgmann et al 1998a, Rosen et al 1998). Rosen et al (1998) succeeded in measuring creep along much of the central aseismic portion of the San Andreas fault in a 14-month interferogram. Surface offsets decrease toward the southeast near the site of the long-awaited Parkfield earthquake. Several short segments of the fault northwest of Parkfield, where no large earthquakes are thought to occur, also showed no evidence of surface offset during this time. This suggests that slip may be accommodated quite episodically in infrequent creep events.

In the San Francisco Bay area, California, where urban development provides for excellent temporal correlation along the Hayward fault, InSAR data allows for detailed measurements along much of the fault (Figure 8, color insert). The Hayward fault slips both episodically, as in a large 1868 $M = 6.8$ earthquake that ruptured the southern 50 km of the fault, and by aseismic creep of the upper few kilometers of the fault at rates of 4–9 mm/year. The range change pattern between 1992 and 1997 shows that the Hayward fault stopped creeping along a previously active 4-km-long segment and experienced transient vertical slip immediately to the northwest (Bürgmann et al 1998a). The transient slip patterns apparently resulted from stress changes due to the 1989 Loma Prieta earthquake south of the Hayward fault.

The northern portion of the Hayward fault has not ruptured in a large earthquake in more than 220 years, which suggests a high earthquake hazard. However, it is possible that the fault may be creeping to greater depths and that it is not capable of producing large earthquake ruptures. Joint inversions of the 5-year interferogram together with available GPS data suggest that this fault may indeed aseismically relieve much of its slip potential (Bürgmann et al 1998b). InSAR data in combination with precise GPS point measurements promise to provide substantially improved determinations of interseismic strain accumulation along active faults, which will allow for better characterization of their earthquake potential.

Volcano Deformation

Volcanic eruptions represent a significant hazard to surrounding communities, and associated ash clouds can endanger air traffic. As opposed to earthquakes, where precursory phenomena that would allow an early warning and response are unreliable, volcanic eruptions are commonly preceded by stages of increasing unrest and characteristic deformation patterns reflecting the ascent of magma through the volcanic edifice. As many as 1000 volcanoes on Earth are considered to be potentially active (about half of which have had historic eruptions), and a significant number are located in areas of high population density. Typically, about 50 volcanoes are active each year. Only a small fraction of hazardous volcanoes are

active at any given time, and only a handful can be routinely monitored with GPS or terrestrial methods. Thus, routine monitoring of volcanic activity through a remote sensing method like InSAR is particularly advantageous. Francis (1999) and Zebker et al (1999) present discussions of InSAR remote sensing of active volcanoes.

Once an eruption takes place, a volcano is difficult to monitor using direct field methods because operation of field equipment is hazardous. When a volcanic episode commences, deformation is commonly rapid and spatially complex. Deformation of volcanic systems includes both faulting and deformation caused by the motion of magma and geothermal fluids in the subsurface that might occur over a wide region surrounding a central volcano. These characteristics make InSAR particularly suitable for investigations of volcano deformation. InSAR allows for remote and hands-off monitoring of many of the Earth's volcanoes. Currently, SAR images are acquired at about monthly intervals, which allows for routine repeated measurements but prevents an immediate response to a sudden volcanic event and detailed monitoring during the days and hours preceding an eruption. Thus, InSAR is probably most useful for long-term global volcano monitoring, to be complemented with continuous GPS point measurements and with seismic and geochemical monitoring, when unrest commences.

InSAR is well suited to measure the complex deformation fields associated with intruding dikes, inflating or deflating magma chambers, and geothermal systems, as well as faulting and slumping of volcanic systems. Because much volcanic deformation is accompanied by significant vertical displacements, InSAR is particularly useful for such investigations. Already, a number of successful volcano deformation studies provide some unusual and promising results. These include investigations of Mount Etna, Italy (Massonnet et al 1995, Lanari et al 1998), Pu'u O'o on Hawaii (Rosen et al 1996), several active Alaskan volcanoes (Lu et al 1997, Lu & Freymueller 1998), rifting and volcanism on Iceland (Sigmundsson et al 1997, Vadon & Sigmundsson 1997), localized inflation on Izu Peninsula, Japan (Fujiwara et al 1998a), dike intrusions on Fernandina volcano, Galapagos (Jónsson et al 1999) and Piton de la Fournaise volcano on La Reunion island (Sigmundsson et al 1999), and deformation of the active calderas of Yellowstone (Wicks et al 1998) and Long Valley (Thatcher & Massonnet 1997, Simons et al 1998). Zebker et al (1999) present interferograms of 16 other recently active volcanoes that nicely illustrate the promises and challenges of InSAR for comprehensive monitoring the Earth's volcanoes.

The first InSAR investigation of volcanic deformation was undertaken using ERS images of Mount Etna, one of the most active volcanoes in the world (Massonnet et al 1995). The analysis of 32 ascending-orbit (satellite moving northward) and 60 descending-orbit interferograms allowed Massonnet et al (1995) to produce 12 satisfactory interferograms showing volcano-wide, steady deflation of about 11 cm during an eruptive episode of Mount Etna that ended in March of 1993. Simple models of a deflating volume source in an elastic half-space suggest that the eruption was fed from a magma chamber 13–19 km deep, emptied

by about $3 \times 10^8 \text{ m}^3$. Using the same interferograms, Briole et al (1997) find that an anomalous zone of enhanced subsidence on the eastern flank of the volcano represents compaction of 3- to 5-year-old lava flows and viscous relaxation of the underlying substrate. Lanari et al (1998) extend the InSAR analysis of Mount Etna through 1996, spanning a phase of inflation following the 1993 eruption. Their models show a shallower, 9-km-deep deflation source in 1993 and a deeper zone of inflation in the years preceding an eruption in late 1995. Using essentially the same modeling approach taken by Massonnet et al (1995), they suggest that their shallower source depths might stem from the use of a more precise DEM. Uplift apparently accelerated in the months preceding the eruption (Figure 9). While the studies of Mount Etna represent a successful demonstration of InSAR for volcano monitoring, these investigations also emphasize the possible effects from DEM errors, the occurrence of atmospheric artifacts that can mimic volcanic deformation (Delacourt et al 1998), severe loss of coherence in particular for the daytime, descending orbit data (Massonnet et al 1995), and the need for more

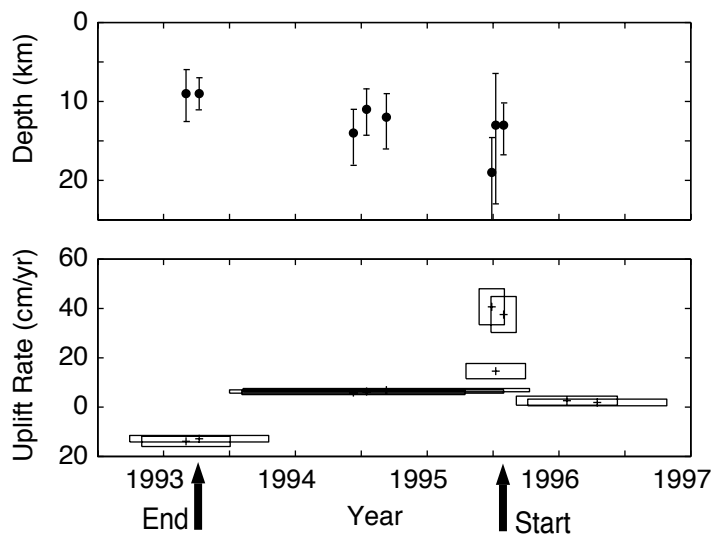


Figure 9 Depth of modeled volume point source and uplift rates from repeated interferograms spanning a deflation-inflation cycle of Mount Etna (modified from Lanari et al 1998). (*Top*) The best fitting depth for eight interferograms used in that study, with error bars representing one standard deviation of the depth estimates. (*Bottom*) Uplift rates deduced from interferograms spanning varying time periods, indicated by the width of the boxes. Note that the InSAR data show subsidence during an eruption that ended in 1993 (arrow labeled “End”), uplift in the 2 years preceding the next volcanic episode that accelerated in the months before the eruption (arrow labeled “Start”), and little deformation in the subsequent year of ongoing eruptive activity.

sophisticated deformation models that account for more realistic representation of the volcanic processes (Cayol & Cornet 1998, Williams & Wadge 1998).

Deformation around many volcanoes is spread out and complex, with eruptions often occurring in rift zones or concentric and radial vent systems at some distance from the central volcano. Thus, it is especially difficult to capture and measure deformation associated with intrusive and extrusive events using traditional means. Two recent studies of active dike intrusion events demonstrate the great utility of InSAR for volcano deformation studies and reveal some interesting and unexpected deformation patterns (Jónsson et al 1999, Sigmundsson et al 1999).

At Fernandina, recent eruptions occurred both in the central caldera and along radial fissures emanating from the volcano (Figure 4). A 1995 eruption from a radial vent system dominates the deformation pattern observed in a 1992–1997 ERS interferogram studied by Jónsson et al (1999) (Figure 10, color insert). The range change pattern consists of a semicircular region of 27 fringes indicating range decrease or uplift to the southeast of the eruptive fissure. Formal nonlinear model inversions for the geometry and magnitude of an underlying dike convincingly show that the intrusion occurred along a shallowly ($\sim 35^\circ$) southeast-dipping fracture. Principal stresses are commonly expected to be parallel or perpendicular to the shear-stress-free surface of the Earth, and dikes were thought to be vertical at Fernandina (Chadwick & Dietrich 1995). The shallow dip of the Fernandina dike intrusion shows that the minimum compressional stress, which is generally perpendicular to dikes, must be rotated about a horizontal axis at least at the shallow depths of the radial rift intrusion. Unfortunately, only one suitable interferogram spanning 5 years exists, so InSAR currently is limited in resolving deformation leading up to or following volcanic intrusions and eruptions; this suggests the need for more frequent data acquisitions with suitable orbital baselines.

Two large caldera systems in North America—Long Valley caldera in California and Yellowstone caldera in Wyoming—were the centers of catastrophic eruptions $>500\text{k}$ years ago but have shown volcanic activity only through minor eruptions since. They are currently locales of high heat flow, geothermal activity, and high rates of seismicity and crustal deformation. The goals of geodetic monitoring of restless caldera systems focus on the detection and correct interpretation of deformation signals related to subsurface movement of magma.

Since the early 1980s, Long Valley has been the site of renewed activity represented in several intermediate-magnitude earthquakes and rapid rates of uplift of the caldera floor; however, no eruptions have taken place for about 250 years (e.g. Rundle & Hill 1988). It is now one of the most closely monitored volcanic regions in the world (e.g. Langbein et al 1995). Thatcher & Massonnet (1997) analyzed two ERS InSAR images that spanned 2 and 4 years, respectively, at Long Valley, using both ascending- and descending-orbit data. The mapped range-change field is consistent overall with that predicted by models of inflating ellipsoidal sources developed from ground-based data (Langbein et al 1995), which indicate a broadly uplifting area rising at ~ 30 mm/year centered on the resurgent

dome of the caldera. Due to their high spatial resolution, the InSAR images also clearly show a small area (~ 1 km across) of subsidence surrounding an actively exploited geothermal field. The InSAR data also indicate additional deformation in an area not otherwise monitored that might be due to intrusive activity to the southwest of the caldera.

At Yellowstone caldera, Wicks et al (1998) used a large number of interferograms to detail a pattern of shifting centers of active swelling and subsidence that is apparently related to continued redistribution of subsurface magma or geothermal activity. These studies already have revealed tantalizing glimpses of the complex nature of these volcanic systems, and InSAR promises to provide a wealth of new information on their subsurface structure, dynamic behavior, and possible hazards.

InSAR appears particularly suited to the study of active volcanic systems because of their relatively rapid, spatially complex deformation patterns and often remote and hazardous environments. Nonetheless, currently available InSAR systems are somewhat limited in their use for volcano monitoring; this is because of their lack of stable orbit control, which makes for inconsistent imaging, rapid temporal decorrelation of InSAR images of vegetated or seasonally snow-covered volcanoes, difficult viewing geometry of steeply flanked stratovolcanoes, enhanced atmospheric artifacts near large volcanoes, and current inability to respond immediately to a volcanic crisis. Future missions that use L-band radar and precise orbit tracking, and that permit the redirection of the radar beam toward particular targets, should remedy many of these limitations and allow for the systematic monitoring and scientific study of the world's active volcanoes.

Land Subsidence

Redistribution of material at shallow levels in the Earth's crust can cause either uplift or subsidence of the surface. In this section, we examine examples of land subsidence and uplift largely related to human activities, as opposed to volcanic and tectonic processes discussed in previous sections.

Subsidence of the land surface is a major global problem, particularly in vulnerable coastal areas. While natural land subsidence affects large areas, those rates are generally slow (except during earthquakes). The removal of subsurface material, such as groundwater, petroleum, or coal, can cause rapid subsidence that affects human activities and infrastructure. Considerable effort and expense are devoted to detection, monitoring, and control of subsidence. Mitigation efforts in the United States alone cost more than \$100 million per year (National Research Council 1991). SAR interferometry has the potential to significantly augment current methods of monitoring in a geographically comprehensive manner, with less frequent ground surveys and on a global basis. Scientists studying tectonic deformation also need to be aware of the large rates of surface deformation related to subsidence to avoid misinterpreting those signals as tec-

tonic. Several recent studies have observed land subsidence with SAR interferometry, all using data from the ERS satellites.

Subsidence due to coal mining has been detected with SAR in Europe, where ancient and modern mining works are present in many areas. Carnec et al (1996) mapped subsidence due to ongoing coal mining at a depth of about 1 km near Gardanne, France. A 35-day interferogram shows a maximum of 42 mm (vertical component) of subsidence directly over the areas mined since 1990. Haynes et al (1997) show total subsidence of up to 78 mm in 2.33 years over ancient coal workings in a location that was not specified, but later revealed to be in Stoke-on-Trent, England (M. Haynes, personal communication). The legal aspects of subsidence are a big concern in many coal-mining areas.

Extraction of fluids (petroleum, gas, or steam) for energy production also causes subsidence in many areas. Massonnet et al (1997) described subsidence over a geothermal field in southern California. Extraction of hot fluid for electricity is causing 10–30 mm per year of subsidence in an area around the field. A 2-year interferogram shows at least two 28.4-mm fringes due to the subsidence, with the center of the subsidence bowl over the southern end of the field (Massonnet et al 1997). A first-order leveling line that passes near the boundary of the field confirms the InSAR measurements, and the net volume of fluid production is comparable to the volume of subsidence measured from the interferogram. Petroleum and gas withdrawal from the Lost Hills and Belridge oil fields in central California has caused rapid subsidence, mapped by Fielding et al (1998). Reservoirs in high-porosity, low-strength diatomite are compacting at shallow (~700 m) depths. A profile through the center of the Lost Hills oil field shows subsidence rates in 1995 that are greater than 1 mm/day (see Figure 11).

Groundwater level variations are by far the most widespread cause of land subsidence (and occasionally uplift or rebound). Rapid extraction of groundwater to supply agriculture or urban areas has caused subsidence in many parts of the world, amounting to several meters in places. Galloway et al (1998) studied land subsidence with InSAR in the Lancaster, California, area, which is undergoing a transition from agriculture to urban land use. Groundwater withdrawal from deep wells has lowered the water levels by 30–90 m from predevelopment levels through 1970. Some parts of the basin have had water level recoveries of up to 15 m since 1970, but the InSAR subsidence map shows up to 50 mm of subsidence over a 26-month period, from October 1993 to December 1995. Ground measurements were not made over that time interval, but the subsidence pattern is largely similar to previous measurements, with some differences. Continued subsidence in areas where water levels have recovered indicates residual compaction due to the earlier water level decline. Hydrologic modeling of water level and hydraulic properties data from wells produces a simulated subsidence pattern that is similar to the observed InSAR pattern (Galloway et al 1998).

Urbanized areas are more vulnerable to damage by land subsidence, but fortunately they are also good places for SAR interferometry because coherence is maintained over long time intervals. In Las Vegas, Nevada, Amelung et al (1999)

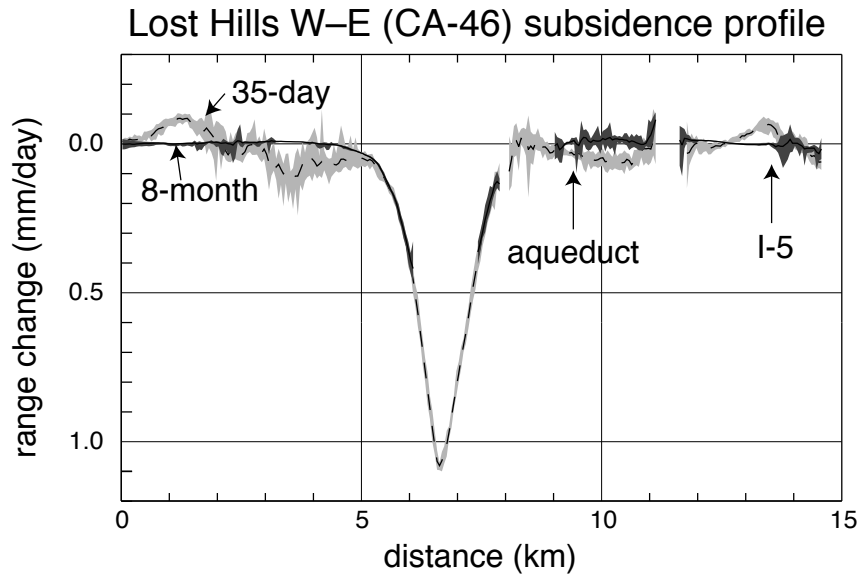


Figure 11 West-east profile through the Lost Hills oil field with the interferometric phase of the 35-day (*light gray and dashed line*) and 8-month (*dark gray and solid line*) pairs converted to range change and divided by the time interval. The graph shows the variation in values (*shaded*) across a 200-m-wide swath through the interferogram, along with the average values (*thick lines*). Gaps are places where the phase could not be unwrapped in the agricultural areas on both interferograms, and in the steep deformation gradients in the center of the oilfield on the 8-month interferogram (modified from Fielding et al 1998).

used InSAR to map subsidence of up to 190 mm over a 5.75-year period. The interferometric subsidence rates from 1992 to 1997 beneath the center of the city are substantially lower than rates before 1990 measured by leveling, which indicates that artificial recharge of aquifers has slowed subsidence but residual subsidence is still occurring. The InSAR subsidence maps also show that subsidence zones in Las Vegas are largely controlled by quaternary faults, a fact not visible on the sparse ground measurements (Amelung et al 1999). In the San Francisco Bay area, two zones show a surprising 40–60 mm of uplift over a 5-year period (Figure 8). Aquifer water levels in the Santa Clara Valley at the south end of the San Francisco Bay have been rising for some time, and this is the most likely cause of this rebound of the surface (Fielding et al 1997). The detailed subsidence or rebound maps possible with InSAR have obvious benefits for water management and monitoring.

THE FUTURE

The next step in topographic mapping will be SRTM. These data will be the first nearly global data set acquired in one epoch and generated with a single reference frame and datum. It will also be the most accurate global-scale topographic product when it is completed in 2001, with 30-m postings and 10- to 15-m height accuracy. The National Imagery and Mapping Agency (NIMA) of the United States is the primary customer for these data, but NASA has an interest in making all data available at degraded (90 m) resolution and some available at full resolution.

There are competing technologies for fine-resolution topographic mapping. Stereo optical systems continue to be attractive because the community is familiar with these data types and the quality of the data can be exceptional. Laser altimeters, with ~ 1 -m height accuracy at ~ 30 -m posting, are becoming increasingly popular; they can profile not only the reflective surface height but also the entire vegetation canopy, giving a close approximation of the ground height and the canopy height as well as the vegetation distribution in the canopy. Despite these optical technologies, topography measurements through radar interferometry will most likely continue to grow. The complete flexibility and control that radar provides with all-weather, day-night observations and the automation of the processing are presently unsurpassed. Airborne dual-antenna interferometers will continue to proliferate as commercial systems that cater to the regional fine-resolution (1- to 5-m posting; 1-m accuracy) mapping community. Spaceborne dual-antenna or dual spacecraft interferometers will also go the next step beyond SRTM, delivering full global coverage, and at finer resolution, perhaps 10-m posting and 5-m accuracy.

For deformation studies, the availability of large amounts of ERS-1/2, JERS-1, and Radarsat data over much of the world has allowed the community to characterize deforming areas and develop methods to interpret these data. The next step is to fly a system that can deliver a data set optimized to the needs of the geophysics community. As we have seen through the descriptions of interferometry methods and the discussion of applications, the full potential of this method has not yet been tapped. The principal limitations are atmospheric distortions of the ground deformation signal, decorrelation limiting accuracy and coverage, and limited availability of radar and supporting data. The next generation of satellites, notably EnviSAT (ESA; multi-mode C-band), RadarSAT 2 (Canadian Space Agency; multi-mode C-band), ALOS (National Space Development Agency, Japan; multi-mode L-band), and LightSAR (NASA; multi-mode L-band) have the opportunity to make observations that will better serve the geophysics community. The satellites should be made to revisit sites of active deformation and observe from several look directions, with fine control of the orbit. The agencies must make these prodigious quantities of data accessible to scientists. The community must develop the next level of analysis tools that

merges multiple data sets and data sources to produce the best derived measurement that suits the science of interest.

The end-of-decade penchant for commercial, military, operational, and scientific multi-use radars, with the eventual goal of commercialization of science data, leads to difficult issues in data access, distribution, and cost. The dynamic environment of the world's growing radar programs is exciting to behold, however. Beyond this coming generation, we can expect dedicated geodetic imaging satellites, the radar equivalents of GPS, to provide continuous monitoring of the Earth's active regions.

The technology of radar interferometry is now mature. For topographic mapping applications, while SRTM and future systems like it must address significant technical challenges—in terms of mast design and metrology, for example—the basic system design and performance have been studied and understood with airborne prototypes. For deformation applications, conventional radar systems with good phase stability are adequate, as demonstrated by existing satellites. Technologies will evolve to allow lower-mass, lower-cost implementations, and innovations in inter-spacecraft communication, orbit control, automated orbit maintenance, and on-board processing could lead to radar platforms flying in formation to serve as reconfigurable interferometry systems for topography and change.

It would also be desirable to bring this technology to other terrestrial planets and moons. Measurements of subtle surface deformations, unencumbered by the kinds of rapid surface changes found on Earth that lead to decorrelation, might yield more readily an understanding of the planetary geodynamics and give greater insight into similar processes on Earth. Detailed surface topography can improve geomorphological interpretations of formation processes. Mars global surveyor laser altimetry on Mars has already done so at coarse resolution (Smith et al 1999). Interferometric measurements with finer resolution, and used on other planets, could be the next frontier of topography and change mapping.

ACKNOWLEDGMENTS

We thank Sigurjon Jónsson, Paul Lundren, Evelyn Price, Scott Rowland, and Gilles Peltzer for providing figures. Falk Amelung, Paul Lundgren, Evelyn Price, Mark Simons, and Tim Wright made helpful comments and suggestions that improved the manuscript. R Bürgmann acknowledges support from National Science Foundation grant EAR-9896297 and grant no. NAG5-7580 from the Solid Earth and Natural Hazards Program Office at NASA. Portions of this paper were written at the Jet Propulsion Laboratory, California Institute of Technology, under contract with the National Aeronautics and Space Administration, with sponsorship from the Solid Earth and Natural Hazards Program Office at NASA.

Visit the Annual Reviews home page at www.AnnualReviews.org.

LITERATURE CITED

- Amelung F, Galloway DL, Bell JW, Zebker HA, Laczniaik RJ. 1999. Sensing the ups and downs of Las Vegas: InSAR reveals structural control of land subsidence and aquifer-system deformation. *Geology* 27:483–86
- Bamler R, Adam N, Davidson GW, Just D. 1998. Noise-induced slope distortion in 2-D phase unwrapping by linear estimators with application to SAR interferometry. *IEEE Trans. Geosci. Remote Sens.* 36:913–21
- Bamler R, Hartl P. 1998. Synthetic aperture radar interferometry. *Inverse Probl.* 14:1–54
- Briole P, Massonnet D, Delacourt C. 1997. Postruptive deformation associated with the 1986–87 and 1989 lava flows of Etna detected by radar interferometry. *Geophys. Res. Lett.* 24:37–40
- Bürgmann R, Fielding E, Sukhatme J. 1998a. Slip along the Hayward fault, California, estimated from space-based SAR interferometry. *Geology* 26:559–62
- Bürgmann R, Segall P, Lisowski M, Svarc J. 1997. Postseismic strain following the 1989 Loma Prieta earthquake from GPS and leveling measurements. *J. Geophys. Res.* 102:4933–55
- Bürgmann R, Sukhatme J, Fielding E. 1998b. Seismic potential of the northern Hayward fault from space based SAR Interferometry and GPS measurements. *EOS Trans. AGU* 79:36 (Abstr.)
- Carnec C, Massonnet D, King C. 1996. Two examples of the use of SAR interferometry on displacement-fields of small spatial extent. *Geophys. Res. Lett.* 23:3579–82
- Cayol V, Cornet FH. 1998. Effects of topography on the interpretation of the deformation field of prominent volcanoes—application to Etna. *Geophys. Res. Lett.* 25:1979–82
- Chadwick WW, Dietrich JH. 1995. Mechanical modeling of circumferential and radial dike intrusions on Galapagos volcanoes. *J. Volcan. Geotherm. Res.* 66:37–52
- Cohee BP, Beroza GC. 1994. Slip distribution of the 1992 Landers earthquake and its implications for earthquake source mechanics. *Bull. Seismol. Soc. Am.* 86:692–712
- Coltelli M, Fornaro G, Franceschetti G, Lanari R, Migliaccio M, et al. 1996. SIR-C/X-SAR multifrequency multipass interferometry—a new tool for geological interpretation. *J. Geophys. Res.* 101:23127–48
- Curlander JC, McDonough RN. 1991. *Synthetic Aperture Radar: Systems and Signal Processing*. New York: Wiley-Intersci. 647 pp.
- Delacourt C, Briole P, Achache J. 1998. Tropospheric corrections of SAR interferograms with strong topography. Application to Etna. *Geophys. Res. Lett.* 25:2849–52
- Deng J, Gurnis M, Kanamori H, Hauksson E. 1998. Viscoelastic flow in the lower crust after the 1992 Landers, California, earthquake. *Science* 282:1689–92
- Dixon TH. 1991. An introduction to the global positioning system and some geological applications. *Rev. Geophys.* 29:249–76
- Elachi C. 1988. *Spaceborne Radar Remote Sensing: Applications and Techniques*. New York: IEEE. 255 pp.
- Evans DL, Farr TG, Zebker HA, van Zyl JJ, Mouginiis-Mark PJ. 1993. Radar interferometry studies of the Earth's topography. *EOS Trans. AGU* 73:553, 557–58
- Feigl KL, Sergent A, Jacq D. 1995. Estimation of an earthquake focal mechanism from a satellite radar interferogram: application to the December 4, 1992 Landers aftershock. *Geophys. Res. Lett.* 22:1037–40

- Fielding EJ. 1999. Morphotectonics of the Himalayas and Tibetan Plateau. In *Geomorphology and Global Tectonics*, ed. MA Summerfield. New York: Wiley. In press
- Fielding EJ, Blom RG, Evans DE, Bürgmann R. 1997. Distinguishing ground subsidence due to subsurface material removal from vertical tectonic motions with SAR interferometry. *EOS Trans. AGU* 78:141 (Abstr.)
- Fielding EJ, Blom RG, Goldstein RM. 1998. Rapid subsidence over oil fields measured by SAR interferometry. *Geophys. Res. Lett.* 25:3215–18
- Francis P. 1999. Remote sensing of active volcanoes. *Annu. Rev. Earth Planet. Sci.* 28:81–106
- Frey Mueller J, King NE, Segall P. 1994. The co-seismic slip distribution of the Landers earthquake. *Bull. Seism. Soc. Am.* 84:646–59
- Fujiwara S, Rosen PA, Tobita M, Murakami M. 1998a. Crustal deformation measurements using repeat-pass JERS 1 synthetic aperture radar interferometry near the Izu Peninsula, Japan. *J. Geophys. Res.* 103:2411–26
- Fujiwara S, Yurai H, Ozawa S, Tobita M, Murakami M, et al. 1998b. Surface displacement of the March 26, 1997 Kagoshima-Kenhokuseibu earthquake in Japan from synthetic aperture radar interferometry. *Geophys. Res. Lett.* 25:4541–44
- Gabriel AK, Goldstein RM. 1988. Crossed orbit interferometry—theory and experimental results from SIR-B. *Int. J. Remote Sens.* 9:857–72
- Gabriel AK, Goldstein RM, Zebker HA. 1989. Mapping small elevation changes over large areas—differential radar interferometry. *J. Geophys. Res.* 94:9183–91
- Galloway DL, Hudnut KW, Ingebritsen SE, Phillips SP, Peltzer G, et al. 1998. Detection of aquifer system compaction and land subsidence using interferometric synthetic-aperture radar, Antelope Valley, Mojave Desert, California. *Water Resour. Res.* 34:2573–85
- Gens R, Vangenderen JL. 1996. SAR interferometry—issues, techniques, applications. *Int. J. Remote Sens.* 17:1803–35
- Ghiglia DC, Pritt MD. 1998. Two-dimensional phase unwrapping: theory, algorithms, and software. New York: Wiley-Intersci. 493 pp.
- Ghiglia DC, Romero G. 1989. Direct phase estimation from phase differences using fast elliptic partial differential equation solvers. *Opt. Lett.* 15:1107–9
- Goldstein R. 1995. Atmospheric limitations to repeat-track radar interferometry. *Geophys. Res. Lett.* 22:2517–20
- Goldstein RM, Engelhardt H, Kamb B, Frolich RM. 1993. Satellite radar interferometry for monitoring ice sheet motion—application to an Antarctic ice stream. *Science* 262:1525–30
- Goldstein RM, Zebker HA. 1987. Interferometric radar measurement of ocean surface currents. *Nature* 328:707–9
- Goldstein RM, Zebker HA, Werner CL. 1988. Satellite radar interferometry—two-dimensional phase unwrapping. *Radio Sci.* 23:713–20
- Graham LC. 1974. Synthetic interferometric radar for topographic mapping. *Proc. IEEE* 62:763–68
- Griffiths H. 1995. Interferometric synthetic aperture radar. *Electron. Commun. Eng. J.* Dec., pp. 247–56
- Hager BH, King RW, Murray MH. 1991. Measurements of crustal deformation using the Global Positioning System. *Annu. Rev. Earth Planet. Sci.* 19:351–82
- Harris R, Segall P. 1987. Detection of a locked zone at depth on the Parkfield, California segment of the San Andreas fault. *J. Geophys. Res.* 92:7945–62
- Haynes M, Capes R, Lawrence G, Smith A, Shilston D, Nicholls G. 1997. Major urban subsidence mapped by differential SAR Interferometry. *Proc. Third ERS Symp. Space Serv. Environ., Florence, Italy, 17–21 March, (ESA SP-414)*, 1:573–77
- Hernandez B, Cotton F, Campillo M, Massonet D. 1997. A comparison between short

- term (co-seismic) and long term (one year) slip for the Landers earthquake: measurements from strong motion and SAR interferometry. *Geophys. Res. Lett.* 24:1579–82
- Hudnut KW, et al. 1994. Co-seismic displacements of the 1992 Landers earthquake sequence. *Bull. Seismol. Soc. Am.* 84:625–45
- Jónsson S, Zebker H, Cervelli P, Segall P, Garbeil H, et al. 1999. A shallow-dipping dike fed the 1995 flank eruption at Fernandina Volcano, Galápagos, observed by Satellite radar interferometry. *Geophys. Res. Lett.* 26:1077–80
- Joughin IR, Winebrenner DP, Percival DB. 1994. Probability density functions for multi-look polarimetric signatures. *IEEE Trans. Geosci. Remote Sens.* 32:562–74
- Lanari R, Lundgren P, Sansosti E. 1998. Dynamic deformation of Etna volcano observed by satellite radar interferometry. *Geophys. Res. Lett.* 25:1541–44
- Langbein J, Dzurisin D, Marshall G, Stein R, Rundle J. 1995. Shallow and peripheral volcanic sources of inflation revealed by modeling two-color geodimeter and leveling data from Long Valley caldera, California, 1988–1992. *J. Geophys. Res.* 100:12487–95
- Lee JS, Hoppel KW, Mango SA, Miller AR. 1992. Intensity and phase statistics of multilook polarimetric and interferometric SAR imagery. *IEEE Trans. Geosci. Remote Sens.* 32:1017–28
- Lin Q, Vesecky JF, Zebker HA. 1994. Phase unwrapping through fringe-line detection in synthetic-aperture radar interferometry. *Appl. Opt.* 33:201–8
- Lu Z, Fatland R, Wyss M, Li S, Eichelberger J, et al. 1997. Deformation of New Trident volcano measured by ERS-1 SAR interferometry, Katmai National Park, Alaska. *Geophys. Res. Lett.* 24:695–98
- Lu Z, Freymueller JT. 1998. Synthetic aperture radar interferometry coherence analysis over Katmai volcano group, Alaska. *J. Geophys. Res.* 103:29887–94
- MacKay ME, Rowland SK, Mouginiis-Mark PJ, Garbeil H. 1998. Thick lava flows of Karisimbi Volcano, Rwanda: insights from SIR-C interferometric topography. *Bull. Volc.* 60:239–51
- Madsen SN, Martin JM, Zebker HA. 1995. Analysis and evaluation of the NASA/JPL TOPSAR across-track interferometric SAR system. *IEEE Trans. Geosci. Remote Sens.* 33:383–91
- Madsen SN, Zebker HA. 1999. Imaging radar interferometry. In *Principles and Applications of Imaging Radar, Manual of Remote Sensing*, 2:359–80. New York: Wiley. 2nd ed.
- Massonnet D, Briole P, Arnaud A. 1995. Deflation of Mount Etna monitored by spaceborne radar interferometry. *Nature* 375:567–70
- Massonnet D, Feigl K, Rossi M, Adragna F. 1994. Radar interferometric mapping of deformation in the year after the Landers earthquake. *Nature* 369:227–30
- Massonnet D, Feigl KL. 1995a. Discrimination of geophysical phenomena in satellite radar interferograms. *Geophys. Res. Lett.* 22:1537–40
- Massonnet D, Feigl KL. 1995b. Satellite radar interferometry map of the coseismic deformation field of the M = 6.1 Eureka Valley, California, earthquake of May 17, 1993. *Geophys. Res. Lett.* 22:1541–44
- Massonnet D, Feigl KL. 1998. Radar interferometry and its application to changes in the earth's surface. *Rev. Geophys.* 36:441–500
- Massonnet D, Feigl KL, Vadon H, Rossi M. 1996a. Coseismic deformation field of the m = 6.7 Northridge, California earthquake of January 17, 1994 recorded by 2 radar satellites using interferometry. *Geophys. Res. Lett.* 23:969–72
- Massonnet D, Holzer T, Vadon H. 1997. Land subsidence caused by the East Mesa Geothermal Field, California, observed using SAR interferometry. *Geophys. Res. Lett.* 24:901–4
- Massonnet D, Rossi M, Carmona C, Adragna F, Peltzer G, et al. 1993. The displacement

- field of the Landers earthquake mapped by radar interferometry. *Nature* 364:138–42
- Massonnet D, Thatcher W, Vadon H. 1996b. Detection of postseismic fault-zone collapse following the Landers earthquake. *Nature* 382:612–16
- Meyer B, Armijo R, Massonnet D, Dechabalier JB, Delacourt C, et al. 1996. The 1995 Grevena (Northern Greece) Earthquake—fault model constrained with tectonic observations and SAR interferometry. *Geophys. Res. Lett.* 23:2677–80
- Mouginis-Mark PJ, Garbeil H. 1993. Digital topography of volcanos from radar interferometry—an example from Mt. Vesuvius, Italy. *Bull. Volcan.* 55:566–70
- Mouginis-Mark PJ, Rowland SK, Garbeil H. 1996. Slopes of western Galapagos volcanoes from airborne interferometric radar. *Geophys. Res. Lett.* 23:3767–70
- Murakami M, Tobita M, Fujiwara S, Saito T, Masaharu H. 1996. Coseismic crustal deformations of 1994 Northridge, California, earthquake detected by interferometry. *J. Geophys. Res.* 101:8605–14
- Murray MH, Savage JC, Lisowski M, Gross WK. 1993. Coseismic displacements: 1992 Landers, California, earthquake. *Geophys. Res. Lett.* 20:623–26
- National Research Council. 1991. *Mitigating Losses from Land Subsidence in the United States*. Washington, DC: Natl. Acad. Sci. 58 pp.
- Ozawa S, Murakami M, Fujiwara S, Tobita M. 1997. Synthetic aperture radar interferogram of the 1995 Kobe earthquake and its geodetic inversion. *Geophys. Res. Lett.* 24:2327–30
- Peltzer G, Crampé F, Hensley S. 1998a. Elastic strain accumulation along the Mojave section of the San Andreas fault, California observed with InSAR. *EOS Trans. AGU* 79:33 (Abstr.)
- Peltzer G, Hudnut KW, Feigl KL. 1994. Analysis of coseismic surface displacement gradients using radar interferometry—new insights into the Landers earthquake. *J. Geophys. Res.* 99:21971–81
- Peltzer G, Rosen P. 1995. Surface displacements of the 17 May 1993 Eureka Valley, California, earthquake observed by SAR interferometry. *Science* 268:1333–36
- Peltzer G, Rosen P, Rogez F, Hudnut K. 1996. Postseismic rebound in fault step-overs caused by pore fluid-flow. *Science* 273:1202–4
- Peltzer G, Rosen P, Rogez F, Hudnut K. 1998b. Poroelastic rebound along the Landers 1992 earthquake surface rupture. *J. Geophys. Res.* 103:30131–45
- Pollitz FF, Peltzer G, Bürgmann R. 2000. Mobility of continental mantle: evidence from postseismic geodetic observations following the 1992 Landers earthquake. *J. Geophys. Res.* In press.
- Price EJ, Sandwell DT. 1998. Small-scale deformations associated with the 1992 Landers, California, earthquake mapped by synthetic aperture radar interferometry phase gradients. *J. Geophys. Res.* 103:27001–16
- Pritchard M, Simons M, Lohman R, Chapin E, Rosen PA, Webb FH. 1998. Constraints on crustal deformation in northern Chile using interferometric synthetic aperture radar. *EOS Trans. AGU* 79:184 (Abstr.)
- Rodriguez E, Martin JM. 1992. Theory and design of interferometric synthetic-aperture radars. *Proc. IEEE* 139(2):147–59
- Rosen PA, Hensley S, Joughin IR, Li F, Madsen SN, et al. 2000. Synthetic aperture radar interferometry. *Proc. IEEE*. In press
- Rosen PA, Hensley S, Zebker HA, Webb FH, Fielding EJ. 1996. Surface deformation and coherence measurements of Kilauea Volcano, Hawaii, from SIR-C radar interferometry. *J. Geophys. Res.* 101:23109–25
- Rosen PA, Werner C, Fielding EJ, Hensley S, Buckley S, Vincent P. 1998. Aseismic creep along the San Andreas fault at Parkfield, California, measured by radar interferometry. *Geophys. Res. Lett.* 25:825–28
- Rowland SK. 1996. Slopes, lava flow volumes, and vent distributions on Volcan Fernandina, Galapagos Islands. *J. Geophys. Res.* 101:27657–72

- Rumsey HC, Morris GA, Green RR, Goldstein RM. 1974. A radar brightness and altitude image of a portion of Venus. *Icarus* 23:1–7
- Rundle JB, Hill DP. 1988. The geophysics of a restless caldera. *Annu. Rev. Earth Planet. Sci.* 16:251–71
- Sandwell DT, Price EJ. 1998. Phase gradient approach to stacking interferograms. *J. Geophys. Res.* 103:30183–204
- Savage JC, Svarc JL. 1997. Postseismic deformation associated with the 1992 Mw = 7.3 Landers earthquake, southern California. *J. Geophys. Res.* 102:7565–77
- Segall P, Davis JL. 1997. GPS applications for geodynamics and earthquake studies. *Annu. Rev. Earth Planet. Sci.* 25:301–36
- Shen ZK, Jackson DD, Feng Y, Cline M, Kim M, et al. 1994. Postseismic deformation following the Landers earthquake, California, 28 June 1992. *Bull. Seism. Soc. Am.* 84:780–91
- Sigmundsson F, Durand P, Massonnet D. 1999. Opening of an eruptive fissure and seaward displacement at Piton de la Fournaise volcano measured by RADARSAT satellite radar interferometry. *Geophys. Res. Lett.* 26:533–36
- Sigmundsson F, Vadon H, Massonnet D. 1997. Readjustment of the Krafla spreading segment to crustal rifting measured by satellite radar interferometry. *Geophys. Res. Lett.* 24:1843–46
- Simons M, Lohman R, Chapin E, Hensley S, Rosen PA, et al. 1998. Sources of deformation in Long Valley caldera. *EOS Trans. AGU* 79:963 (Abstr.)
- Smith DE, Zuber MT, Solomon SC, Phillips RJ, Head JW, et al. 1999. The global topography of Mars and implications for surface evolution. *Science* 184:1495–503
- Tarayre H, Massonnet D. 1996. Atmospheric propagation heterogeneities revealed by ERS-1 interferometry. *Geophys. Res. Lett.* 23:989–92
- Thatcher W. 1983. Nonlinear strain buildup and the earthquake cycle on the San Andreas fault. *J. Geophys. Res.* 88:5893–902
- Thatcher W. 1986. Cyclic deformation related to great earthquakes at plate boundaries. *R. Soc. NZ Bull.* 24:245–72
- Thatcher W, Massonnet D. 1997. Crustal deformation at Long Valley Caldera, eastern California, 1992–1996 inferred from satellite radar interferometry. *Geophys. Res. Lett.* 24:2519–22
- Tobita M, Fujiwara S, Ozawa S, Rosen PA, Fielding EJ, et al. 1998. Deformation of the 1995 North Sakhalin earthquake detected by JERS-1/SAR interferometry. *Earth Planets Space* 50:313–25
- USGS. 1993. *Digital Elevation Models, Data Users Guide 5*. Reston, VA: USGS. 51 pp.
- Vadon H, Sigmundsson F. 1997. Crustal deformation from 1992 to 1995 at the Mid-Atlantic ridge, southwest Iceland, mapped by satellite radar interferometry. *Science* 275:193–97
- Wald DJ, Heaton TH. 1994. Spatial and temporal distribution of slip for the 1992 Landers, California earthquake. *Bull. Seismol. Soc. Am.* 86:668–91
- Wicks C, Thatcher W, Dzurisin D. 1998. Migration of fluids beneath Yellowstone caldera inferred from satellite radar interferometry. *Science* 282:458–62
- Williams CA, Wadge G. 1998. The effects of topography on magma chamber deformation models: application to Mt. Etna and radar interferometry. *Geophys. Res. Lett.* 25:1549–52
- Williams S, Bock Y, Fang P. 1998. Integrated satellite interferometry: tropospheric noise, GPS estimates and implications for interferometric synthetic aperture radar products. *J. Geophys. Res.* 103:27051–67
- Wright TJ, Parsons BE, Jackson JA, Haynes A, Fielding EJ, et al. 1999. Source parameters of the 1 October 1995 Dinar (Turkey) earthquake from SAR interferometry and seismic body wave modelling. *Earth Planet. Sci. Lett.* 179:23–37
- Zebker H, Amelung F, Jónsson S. 1999. Remote sensing of volcano surface and internal processes using radar interferometry.

- try. *AGU Monogr. Remote Sens. Act. Volcanoes*. In press
- Zebker HA, Goldstein RM. 1986. Topographic mapping from interferometric SAR observations. *J. Geophys. Res.* 91:4993–99
- Zebker HA, Lu YP. 1998. Phase unwrapping algorithms for radar interferometry: residue-cut, least-squares, and synthesis algorithms. *J. Opt. Soc. Am. A Opt. Image Sci. Vis.* 15:586–98
- Zebker HA, Madsen SN, Martin J, Wheeler KB, Miller T, et al. 1992. The TOPSAR interferometric radar topographic mapping instrument. *IEEE Trans. Geosci. Remote Sens.* 30:933–40
- Zebker HA, Rosen PA, Goldstein RM, Gabriel A, Werner CL. 1994. On the derivation of coseismic displacement fields using differential radar interferometry—the Landers earthquake. *J. Geophys. Res.* 99:19617–34
- Zebker HA, Rosen PA, Hensley S. 1997. Atmospheric effects in interferometric synthetic aperture radar surface deformation and topographic maps. *J. Geophys. Res.* 102:7547–63
- Zebker HA, Villasenor J. 1992. Decorrelation in interferometric radar echoes. *IEEE Trans. Geosci. Remote Sens.* 30:950–59
- Zisk SH. 1972. Lunar topography: first radar-interferometer measurements of the Alphonsus-Ptolemaeus-Arzachel region. *Science* 178:977–80



CONTENTS

Palynology after Y2K--Understanding the Source Area of Pollen in Sediments, <i>M. B. Davis</i>	1
Dinosaur Reproduction and Parenting, <i>John R. Horner</i>	19
Evolution and Structure of the Lachlan Fold Belt (Orogen) of Eastern Australia, <i>David A. Foster, David R. Gray</i>	47
Remote Sensing of Active Volcanoes, <i>Peter Francis, David Rothery</i>	81
Dynamics of Volcanic Systems in Iceland: Example of Tectonism and Volcanism at Juxtaposed Hot Spot and Mid-Ocean Ridge Systems, <i>Agust Gudmundsson</i>	107
Understanding Oblique Impacts from Experiments, Observations, and Modeling, <i>E. Pierazzo, H. J. Melosh</i>	141
Synthetic Aperture Radar Interferometry to Measure Earth's Surface Topography and Its Deformation, <i>Roland Bürgmann, Paul A. Rosen, Eric J. Fielding</i>	169
Geologic Evolution of the Himalayan-Tibetan Orogen, <i>An Yin, T. Mark Harrison</i>	211
MARS 2000, <i>Arden L. Albee</i>	281
Vredefort, Sudbury, Chicxulub: Three of a Kind, <i>Richard Grieve, Ann Therriault</i>	305
Climate Reconstruction from Subsurface Temperatures, <i>Henry N. Pollack, Shaopeng Huang</i>	339
Asteroid Fragmentation and Evolution of Asteroids, <i>Eileen V. Ryan</i>	367
Seismic Imaging of Mantle Plumes, <i>Henri-Claude Nataf</i>	391
New Perspectives on Orbitally Forced Stratigraphy, <i>Linda A. Hinnov</i>	419
Clathrate Hydrates, <i>Bruce A. Buffett</i>	477
Heterogeneity of the Lowermost Mantle, <i>Edward J. Garnero</i>	509
Spreading Volcanoes, <i>Andrea Borgia, Paul T. Delaney, Roger P. Denlinger</i>	539
Scaling, Universality, and Geomorphology, <i>Peter Sheridan Dodds, Daniel H. Rothman</i>	571
Chemical Weathering, Atmospheric CO ₂ , and Climate, <i>Lee R. Kump, Susan L. Brantley, Michael A. Arthur</i>	611
Self-Ordering and Complexity in Epizonal Mineral Deposits, <i>Richard W. Henley, Byron R. Berger</i>	669